Comput. Mech. (2007) 39: 859–877
DOI 10.1007/s00466-006-0075-4

ORIGINAL PAPER

G. R. Liu · K. Y. Dai · T. T. Nguyen

A smoothed finite element method for mechanics problems

Received: 28 November 2005 / Accepted: 30 April 2006 / Published online: 17 May 2006
© Springer-Verlag 2006

Abstract In the finite element method (FEM), a necessary condition for a four-node isoparametric element is that no interior angle is greater than 180° and the positivity of Jacobian determinant should be ensured in numerical implementation. In this paper, we incorporate cell-wise strain smoothing operations into conventional finite elements and propose the smoothed finite element method (SFEM) for 2D elastic problems. It is found that a quadrilateral element divided into four smoothing cells can avoid spurious modes and gives stable results for integration over the element. Compared with original FEM, the SFEM achieves more accurate results and generally higher convergence rate in energy without increasing computational cost. More importantly, as no mapping or coordinate transformation is involved in the SFEM, its element is allowed to be of arbitrary shape. Hence the restriction on the shape bilinear isoparametric elements can be removed and problem domain can be discretized in more flexible ways, as demonstrated in the example problems.

Keywords Finite element method (FEM) · Smoothed finite element method (SFEM) · Strain smoothing · Isoparametric element · Gauss quadrature

1 Introduction

After more than half a century of development, finite element method (FEM) has become a very powerful and versatile technique for numerical simulations in engineering and science. Mapped elements, such as the well-known isoparametric elements, play a very important role in FEM. When using a mapped element, a basic requirement is that the element has to be convex and a violent distortion is not permitted so that a one-to-one coordinate correspondence between the physical and natural coordinates associated with the element can be guaranteed. More specifically, for a 2D four-node element using mapped bilinear shape functions, a necessary condition is that any internal angle should not be greater than, theoretically, 180°. In numerical implementation, the determinant of the Jacobian matrix should be always checked for its positivity to avoid severely distorted elements [1, 13, 24]. In addition, in the numerical integration of Galerkin weak form, Gauss quadrature is a commonly used method. Besides the complexity in implementation, quadrature rule required in problem with high-order approximated function will substantially increase the computational cost.

One of the major objectives of the recent development of mesh-free method is to avoid problems related to element distortion encountered in FEM [3, 11], and many useful techniques have been developed so far. Recently, nodal integration method has been suggested in mesh-free methods with the aim to eliminate "background" mesh for integration [2, 5]. Direct nodal integration often suffers from numerical instability and low accuracy. Chen et al. [7] found that the instability is due to the vanishing of derivatives of shape functions at the field nodes and the low accuracy is caused by the violation of the integration constraints (IC) in the Galerkin weak-form formulations. A linear consistent shape function does not necessarily guarantee a linear exactness in the solution of a mesh-free method based on Galerkin weak form, such as the EFG method [4], and RKPM [15]. They proposed a stabilized conforming nodal integration using a strain smoothing technique for a Galerkin mesh-free method and thus the method shows higher efficiency, desired accuracy and convergent properties. Yoo et al. [23] then extended the stabilized nodal integration to the natural-element method and solved the nearly incompressible problems without any modification of integration scheme. Liu et al. [12, 14]

G. R. Liu · K. Y. Dai (✉) · T. T. Nguyen
Center for Advanced Computations in Engineering Science (ACES),
Department of Mechanical Engineering,
National University of Singapore,
10 Kent Ridge Crescent 119260, Singapore, Singapore
E-mail: smadky@nus.edu.sg
Tel.: +65-6516-4796
Fax: +65-6516-4795

G. R. Liu · K. Y. Dai
Singapore-MIT Alliance (SMA),
E4-04-10, 4 Engineering Drive 3,
117576, Singapore, Singapore

introduced the nodal integration into the radial point interpolation method to install linear conformability and good performance has been observed for many problems including contact problems [9].

In the mesh-free methods based on nodal integration, the entire domain is still required to be discretized into cells based on the field nodes for integration purpose, such as Voronoi diagram, and the integrations are performed along the edges of each cell. In addition, despite field function is approximated using high-order shape functions, the computed strains and stresses are still constant within the cell associated with a node. Though mesh-free method has good accuracy and high convergence speed, the complex field approximation inevitably increases the computational cost. Therefore a question naturally arises. Can we project strain smoothing in a finite element onto a constant field or set of constant fields based on further divided cells in an element? If this can be done, volume integrals involving shape function gradients can be recast into surface integrals involving only shape functions. Thus simple shape function, such as linear shape function may be used. As the elements are, in fact, the integration cells in the FEM, the domain integration can be changed to line integration for 2D problems with the introduction of strain smoothing technique. In this work, we implement this idea to formulate and code a novel method, smoothed finite element method (SFEM), which makes use of the existing FEM technology and the strain smoothing technique. We will demonstrate through intensive case studies the significant benefits arising from this novel combination.

The paper is outlined as follows. First the strain smoothing technique proposed by Chen et al. [7] is briefly reviewed. The idea of SFEM and the construction of its shape functions are then presented in Sect. 3. In Sect. 4, numerical implementation issues are discussed with emphasis on division of smoothing cells for stability purpose. Standard patch tests are conducted with elements of extremely distorted shapes. Some numerical examples are analyzed using SFEM in Sect. 5 and the accuracy and convergence rate are compared with FEM. Some concluding remarks are made in the last section.

2 Strain smoothing

A 2D static elasticity problem can be described by equilibrium equation in the domain Ω bounded by Γ and $\Gamma = \Gamma_u + \Gamma_t$, $\Gamma_u \cap \Gamma_t = \emptyset$.

$$\sigma_{ij,j} + b_i = 0 \quad \text{in } \Omega, \tag{1}$$

where σ_{ij} is the component of stress tensor and b_i is the component of body force. Boundary conditions are given as follows.

$$\sigma_{ij} n_j = t_i \quad \text{on } \Gamma_t \tag{2}$$

$$u_i = \bar{u}_i \quad \text{on } \Gamma_u \tag{3}$$

where t_i is the traction on Γ_t; $\bar{u}_i$ denotes the prescribed boundary displacements on Γ_u and n_i is the unit outward normal. Its variational weak form is expressed as

$$\int_\Omega \delta \nabla_s(u)_{ij} D_{ijkl} \nabla_s(u)_{kl} \mathrm{d}\Omega - \int_{\Gamma_t} \delta u_i t_i \mathrm{d}\Gamma = 0, \tag{4}$$

where $\nabla_s \mathbf{u}$ denotes the symmetric part of displacement gradient and D_{ijkl} is material elasticity tensor.

In mesh-free method based on nodal integration form, the above integration is performed over representative cells of nodes in the problem domain [7]. To guarantee the convergence of the solution, the linear exactness in the solution of the weak form should be ensured. To meet the requirement, the following integration constraint should be satisfied [7, 9]

$$\int_\Omega \mathbf{B}_I^{\mathrm{T}}(\mathbf{x}) \mathrm{d}\Omega = \int_{\Gamma_t} \mathbf{N}_I^{\mathrm{T}}(\mathbf{x}) \mathrm{d}\Gamma, \tag{5}$$

where $\mathbf{B}_I$ is the standard gradient matrix as given by

$$\mathbf{B}_I = \begin{bmatrix} N_{I,1} & 0 \\ 0 & N_{I,2} \\ N_{I,2} & N_{I,1} \end{bmatrix}, \quad \mathbf{N}_I = \begin{bmatrix} N_I n_1 & 0 \\ 0 & N_I n_2 \\ N_I n_2 & N_I n_1 \end{bmatrix} \tag{6}$$

The condition is met by using strain smoothing techniques for each representative nodal cell [7].

In this section, we formulate SFEM based on the conventional FEM incorporating the idea of strain smoothing operation used in the mesh-free nodal integration method [6]. The essence of the formulation of SFEM is as follows. (1) Elements are used as in the FEM, but they are allowed to be of polygon or other arbitrary shapes, which can be even concave, as shown in Fig. 7 for example. (2) Galerkin weak form given in Eq. (4) is applied and integration is performed on the basis of element. Depending on the requirement of stability, an element may be further subdivided into several smoothing cells (SC). (3) A smoothing operation is performed for each smoothing cell within an element. When choosing a constant smoothing function, area integration over the cell becomes line integration along its boundaries, and no gradient of shape functions is involved in computing the field gradients as well as in forming the stiffness matrix. The integration along the edges of each cell is performed numerically using 1D Gauss integration scheme. (4) The shape function is created via a simple and explicit manner, which ensures efficiency, consistency and accuracy. Methods used in natural-element method [18, 19] and polygonal finite elements [17, 20] can be introduced here for determination of shape functions of interior points. Approaches widely used in creating mesh-free shape functions are also applicable, including MLS/RK, PIM/RPIM. The formulations are detailed below.

A smoothing operation is performed to the gradient of displacement for each smoothing cells in an element

$$\nabla u^h(\mathbf{x}_C) = \int_\Omega \nabla u^h(\mathbf{x}) \Phi(\mathbf{x} - \mathbf{x}_C) \mathrm{d}\Omega. \tag{7}$$

Integration by parts for the right-hand side leads to

$$\nabla u^h(\mathbf{x}_C) = \int_\Gamma u^h(\mathbf{x})\mathbf{n}(\mathbf{x})\Phi(\mathbf{x}-\mathbf{x}_C)\,\mathrm{d}\Gamma - \int_\Omega u^h(\mathbf{x})\nabla\Phi(\mathbf{x}-\mathbf{x}_C)\mathrm{d}\Omega, \tag{8}$$

where Φ is a smoothing function. For simplicity, a piecewise constant function is applied here, which is assumed to be constant within Ω_C and vanish somewhere else, as given by

$$\Phi(\mathbf{x}-\mathbf{x}_C) = \begin{cases} 1/A_C & \mathbf{x}\in\Omega_C \\ 0 & \mathbf{x}\notin\Omega_C, \end{cases} \tag{9}$$

where $A_C = \int_{\Omega_C}\mathrm{d}\Omega$ and Ω_C is the smoothing cell (see Fig. 3). Note that this kind of smoothing operation was also used in the SPH method [13, 16] for field approximation purpose.

Substituting Φ into Eq. (7), one can get the smoothed gradient of displacement

$$\tilde{\nabla} u^h(\mathbf{x}_C) = \int_{\Gamma_C} u^h(\mathbf{x})\mathbf{n}(\mathbf{x})\Phi(\mathbf{x}-\mathbf{x}_C)\mathrm{d}\Gamma = \frac{1}{A_C}\int_{\Gamma_C} u^h(\mathbf{x})\mathbf{n}(\mathbf{x})\mathrm{d}\Gamma, \tag{10}$$

where Γ_C is the boundary of the smoothing cell. Note that the choice of constant Φ makes vanishing the second term on the right-hand side of Eq. (8) and the area integration becomes line integration along the edges of smoothing cell in Eq. (7). Similarly the smoothed strain can be obtained as given by

$$\tilde{\boldsymbol{\varepsilon}}^h(\mathbf{x}_C) = \sum_{I=1}^{n}\tilde{\mathbf{B}}_I(\mathbf{x}_C)\mathbf{d}_I, \tag{11}$$

where $\tilde{\mathbf{B}}_I$ is the smoothed strain matrix. For 2D case

$$\tilde{\mathbf{B}}_I(\mathbf{x}_C) = \begin{bmatrix} \tilde{b}_{I1}(\mathbf{x}_C) & 0 \\ 0 & \tilde{b}_{I2}(\mathbf{x}_C) \\ \tilde{b}_{I2}(\mathbf{x}_C) & \tilde{b}_{I1}(\mathbf{x}_C) \end{bmatrix}, \tag{12}$$

where

$$\tilde{b}_{Ik}(\mathbf{x}_C) = \frac{1}{A_C}\int_{\Gamma_C} N_I(\mathbf{x})n_k(\mathbf{x})\mathrm{d}\Gamma, \quad (k=1,\ 2) \tag{13a}$$

If one Gaussian point is used for line integration along each segment of boundary Γ_i^C of Ω_C, the above equation can be transformed to its algebraic form

$$\tilde{b}_{Ik}(\mathbf{x}_C) = \sum_{i=1}^{M} N_I(\mathbf{x}_i^{\mathrm{GP}})n_{ik}^C l_i^C, \tag{13b}$$

where $\mathbf{x}_i$ is the midpoint (Gaussian point) of boundary segment of Γ_i^C, whose length and outward unit normal are denoted as l_i^C and n_i^C, respectively.

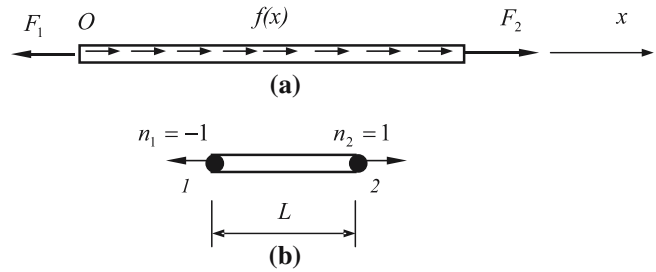

Fig. 1 **a** An elastic rod; **b** a rod element

The smoothed element stiffness matrix can be obtained by assembly of those of all of the smoothing cells of the element, i.e.,

$$\mathbf{K}_e = \sum_C \tilde{\mathbf{B}}_C^{\mathrm{T}}\mathbf{D}\tilde{\mathbf{B}}_C A_C \tag{14}$$

The smoothed $\tilde{\mathbf{B}}_C$ matrices are constructed with an integration over the boundary of the cell c.

Note that it has been proved that the strain smoothing stabilization can exactly satisfy the integration constraints of Eq. (5) [6].

For demonstration purpose, a one-dimensional elastic rod is studied as shown in Fig. 1a. Ignoring the inertia effect, the differential equation governing this problem is expressed as

$$EA\frac{\mathrm{d}^2u}{\mathrm{d}x^2} + f(x) = 0, \tag{15}$$

where E is the Young's modulus and A is the area of the cross-section of the rod. The element stiffness matrix obtained from Galerkin weak form can be easily derived as follows assuming constant EA along the bar

$$\mathbf{K}_e = EA\int_0^L \tilde{\mathbf{B}}^T\tilde{\mathbf{B}}dL\mathrm{d}x = EA\int_0^L \begin{bmatrix}\tilde{B}_1\\ \tilde{B}_2\end{bmatrix}\begin{bmatrix}\tilde{B}_1 & \tilde{B}_2\end{bmatrix}\mathrm{d}x = EA\int_0^L \begin{bmatrix}\frac{\partial N_1}{\partial x}\\ \frac{\partial N_2}{\partial x}\end{bmatrix}\begin{bmatrix}\frac{\partial N_1}{\partial x} & \frac{\partial N_2}{\partial x}\end{bmatrix}\mathrm{d}x, \tag{16}$$

where L is the length of the element and $N_i (i = 1,\ 2)$ is the shape function associated with node i.

If linear shape functions are adopted and one Gauss point is sufficient for integration, the components of $\tilde{\mathbf{B}}$ are calculated using Eq. (12)

$$\tilde{B}_1 = [N_1(0)n_1 + N_1(L)n_2]/L = -1/L$$
$$\tilde{B}_2 = [N_2(0)n_1 + N_2(L)n_2]/L = 1/L.$$

Therefore, the element stiffness matrix is obtained as

$$\mathbf{K}_e = \frac{EA}{L}\begin{bmatrix}1 & -1\\ -1 & 1\end{bmatrix} \tag{17}$$

which coincides with its counterpart in FEM.

Similarly, the element stiffness matrix of a three-node triangular element is also derived with boundary integration

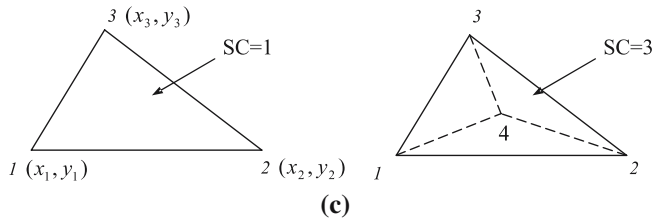

Fig. 2 A 2D triangular element

performed along its sides (See Fig. 2). When linear shape functions are used, the calculated strain matrix is expressed as

$$\tilde{\mathbf{B}}_i = \frac{1}{2A_e}\begin{bmatrix} b_i & 0 \\ 0 & c_i \\ c_i & b_i \end{bmatrix}, \quad (i = 1, 2, 3), \tag{18}$$

where A_e is the area of the element. The coefficients are given by $b_i = y_{i+1} - y_{i+2}$ and $c_i = x_{i-1} - x_{i-2}$. Note that the index is defined recursively in the form of $(1 \to 2 \to 3 \to 1)$. For example, if $i = 2$, we have $i + 1 \Rightarrow 3$, $i + 2 \Rightarrow 1$, $i - 1 \Rightarrow 1$ and $i - 2 \Rightarrow 3$. It can be found once again that the calculated stiffness matrix is identical with three-node triangular elements obtained in the standard FEM. Further division of the element into three or six smoothing cells and assembly of their contribution together lead to the same results due to the constant derivatives of shape functions within an element. The conclusion can be easily extended to any element with constant strains/stresses, that both FEM and SFEM will yield identical stiffness matrix. If we further investigate the stiffness matrix for four-node rectangular element, or more generally, quadrilateral element or polygonal elements, we can find that the SFEM results are quite different from their counterparts in FEM. This will be detailed in the following section.

As recommended by Yoo et al. [23], higher-order gradients can be readily obtained by recursive application of the non-local operator $\tilde{\nabla}$ in Eq. (10). The first order of displacement gradients are rewritten as

$$\tilde{D}^u_{ij}(\mathbf{x}_C) = \frac{\tilde{\partial} u^h_i(\mathbf{x}_C)}{\partial x_j} = \frac{1}{A_C}\int_{\Gamma_C} N_I(\mathbf{x}) n_j(\mathbf{x}) \mathrm{d}\Gamma u_{iI}. \tag{19}$$

As long as $\tilde{\mathbf{D}}^u$ can be interpolated from nodal values, the second order of the displacement gradients can be obtained in the same way

$$\tilde{D}^u_{ijk}(\mathbf{x}_C) = \frac{\tilde{\partial}^2 u^h_i(\mathbf{x}_C)}{\partial x_j \partial x_k} = \frac{1}{A_C}\int_{\Gamma_C} N_I(\mathbf{x}) n_k(\mathbf{x}) \mathrm{d}\Gamma \tilde{D}^u_{ijI}. \tag{20}$$

3 Construction of SFEM shape functions

We may subdivide a quadrilateral element into four smoothing cells and strain smoothing is performed over each cell and "smoothed" cell integration becomes line integration along boundary of the cell.

Table 1 Shape function value at different sites within an element (Fig. 5)

Site	Node 1	Node 2	Node 3	Node 4	Descpription
1	1.0	0	0	0	Field node
2	0	1.0	0	0	Field node
3	0	0	1.0	0	Field node
4	0	0	0	1.0	Field node
5	0.5	0.5	0	0	Side midpoint
6	0	0.5	0.5	0	Side midpoint
7	0	0	0.5	0.5	Side midpoint
8	0.5	0	0	0.5	Side midpoint
9	0.25	0.25	0.25	0.25	Intersection of two bimedians [a]

[a] Note that if this point coincides with a field node, it should adopt the shape function values of this node

Table 2 Eigenvalues of a free solid using one element ($E = 3.0 \times 10^7$, $v = 0.3$)

Eigenvalues	FEM		SFEM	
	1×1 GP	2×2 GPs	SC = 1	SC = 4
1	4.286e7	4.286e7	4.286e7	4.286e7
2	2.308e7	2.308e7	2.308e7	2.308e7
3	2.308e7	2.308e7	2.308e7	2.308e7
4	0	1.484e7	0	1.113e7
5	0	1.484e7	0	1.113e7
6	0	0	0	0
7	0	0	0	0
8	0	0	0	0

Table 3 First eight eigenvalues of a free solid using 4 × 4 element ($E = 3.0 \times 10^7$, $v = 0.3$)

Eigenvalues	FEM		SFEM	
	1×1 GP	2×2 GPs	SC = 1	SC = 4
1	2.770e6	8.439e6	2.770e6	8.291e6
2	2.770e6	6.182e6	2.770e6	6.152e6
3	0	4.408e6	0	4.032e6
4	0	4.160e6	0	3.968e6
5	0	4.160e6	0	3.968e6
6	0	0	0	0
7	0	0	0	0
8	0	0	0	0

Table 4 Eigenvalues of a solid fixed with 3 DOFs using one element ($E = 3.0 \times 10^7$, $v = 0.3$)

Eigenvalues	FEM		SFEM	
	1×1 GP	2×2 GPs	SC = 1	SC = 4
1	3.445e7	3.462e7	3.445e7	3.454e7
2	1.899e7	2.002e7	1.899e7	1.943e7
3	1.632e7	1.784e7	1.632e7	1.724e7
4	0.935	1.148e7	0.935	8.724e6
5	0.707	6.255e6	0.707	4.949e6
6	0.707	0.707	0.707	0.707
7	0	0.707	0	0.707
8	0	0.354	0	0.354

In the SFEM, as only the shape function itself is used to calculate the strain matrix, very simple shape functions can be utilized at Gauss points on the edges of a cell. For any point on edge, e.g., the midpoints #5, #6, #7 and #8 shown in Fig. 7a, the values of the shape functions are calculated using linear shape functions of two related nodes on the edge. The values of the shape functions at point #9, the intersection of

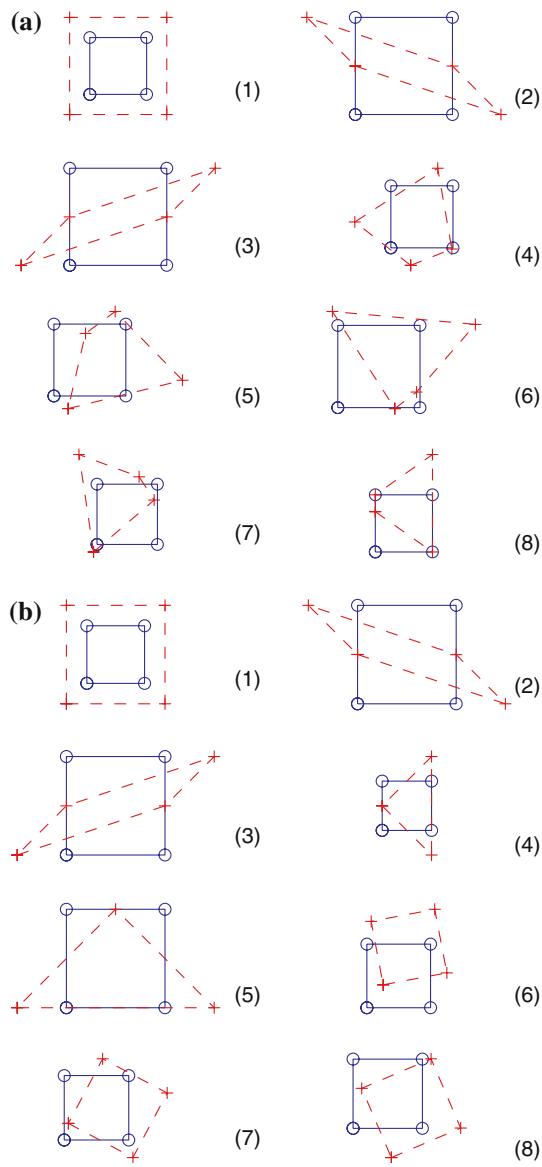

Fig. 3 Eigenmodes of a patch divided into one four-node element. **a** SC = 1 (1 GP); **b** SC = 4 (2 × 2 GPs)

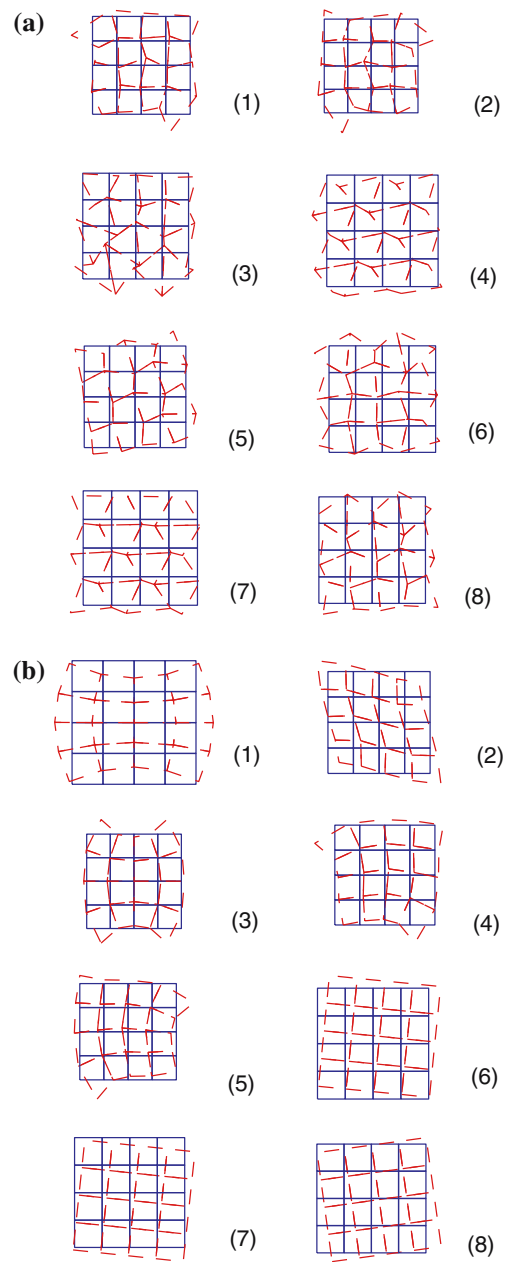

Fig. 4 Eigenmodes of a patch divided into 16 four-node elements. **b** SC = 1 (1 GP); **b** SC = 4 (2 × 2 GPs)

two bimedians, are the average of those at the four midpoints. If this point happens to coincide with one field node, its shape function values should be identical with this node accordingly as occurring in Fig. 7f, for example. Shape functions for other interior points can be easily obtained in a similar way. For clarity, the values of shape functions are listed explicitly in Table 1 for some commonly used points.

For arbitrary interior point $\mathbf{x}_Q(x, y)$, the shape function can be obtained in such a way that

$$N(\mathbf{x}) = \mathbf{p}^{\mathrm{T}}(\mathbf{x})\mathbf{a}, \tag{21}$$

where $\mathbf{x} = [\,x\ y\,]$ in 2D problems, $\mathbf{p}^{\mathrm{T}}(\mathbf{x}) = [\,1\ x\ y\ xy\,]$ is the polynomial bases and $\mathbf{a} = \left[\,a_1\ a_2\ a_3\ a_4\,\right]$ is a vector of the unknown coefficients. Using the Lagrange interpolation, the shape functions can be computed as follows

$$N(\mathbf{x}) = \left[\,1\ x\ y\ xy\,\right] \begin{bmatrix} 1 & x_1 & y_1 & x_1 y_1 \\ 1 & x_2 & y_2 & x_2 y_2 \\ 1 & x_3 & y_3 & x_3 y_3 \\ 1 & x_4 & y_4 & x_4 y_4 \end{bmatrix}^{-1}, \tag{22}$$

where $\mathbf{x}_i = [\,x_i\ y_i\,](i = 1, 2, 3, 4)$ are the coordinates of the four nodes associated with this element. Actually, the shape functions at point #9 for quadrilateral element can also be evaluated using above equation. Unless stated otherwise, we still use the averaged shape functions in Table 1 for following examples for convenience.

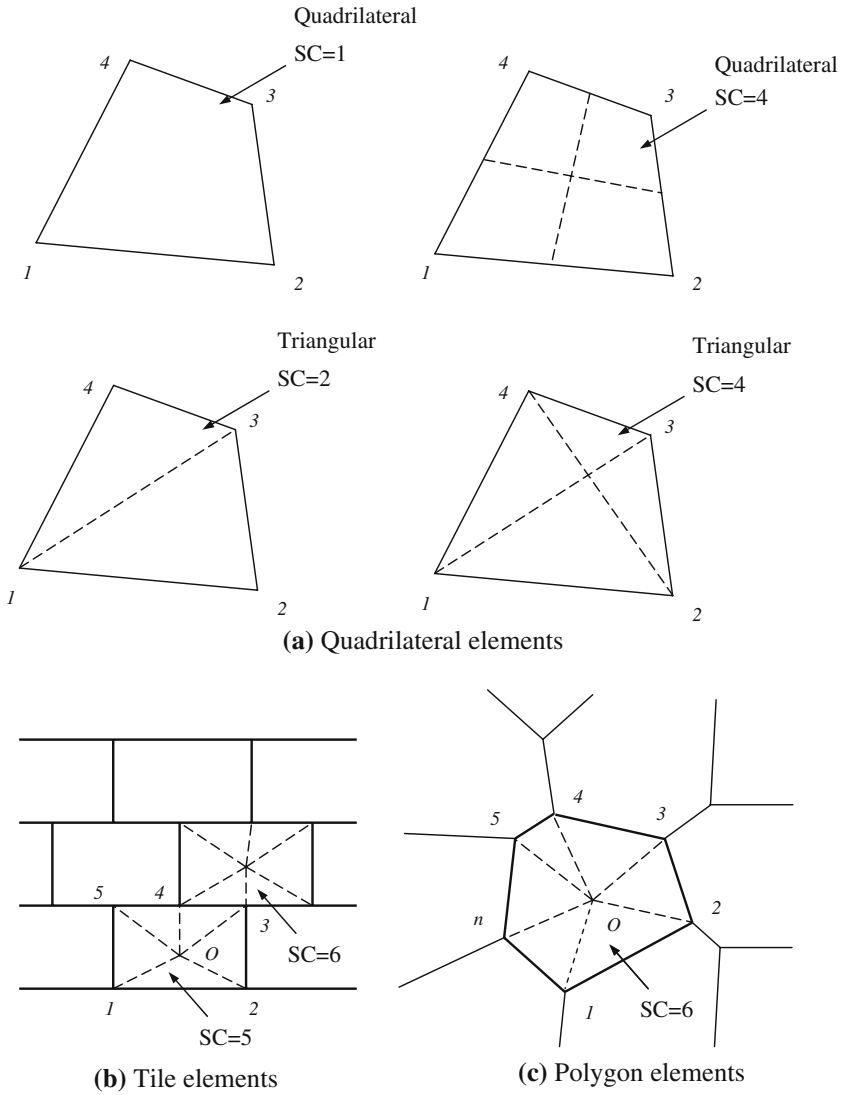

Fig. 5 Mesh structure and smoothing cells. **a** quadrilateral elements; **b** tile elements; **c** polygonal elements

Different from the standard four-node isoparametric finite elements, shape functions obtained above do not use coordinate transformation or mapping. Note that the bilinear property may or may not be preserved for a quadrilateral element with arbitrary shape via above-mentioned procedures. However, the linear geometric conformability can still be ensured. It is clearly seen that shape functions obtained by both method could always satisfy the integration constraints as given in Eq. (5). As the shape function is linearly changed along each side of the smoothing cell, one Gauss point is sufficient for accurate boundary integration.

For a polygonal element with n sides ($n \geq 4$), we can simply divide the element into n triangular smoothing cells. Similarly the shape functions on its boundary are constructed linearly using two related nodes. The shape functions for the interior nodes can be obtained using the natural element method, polygonal finite elements proposed by Sukumar et al. [19, 20], or the mesh-free techniques, such as MLS/RK methods [3, 15], radial point interpolation method (RPIM). It should be mentioned here, though mesh-free techniques are suggested, only nodes associated with the element can be used to derive the shape functions and thus interpolation nodes are limited to the interested element only. To derive RPIM shape functions with linear consistency, note that at least linear polynomials should be included in interpolation bases. Detailed formulations can be found in references [8, 11, 22].

Examining Eqs. (11) through (13), we can see that the smoothed strain matrix $\tilde{\mathbf{B}}$ is not only related to $\mathbf{N}$ and $\mathbf{n}$, but also to A_C, the area of the smoothing cell. For an element, if the areas of the divided smoothing cells are equal, they are indeed cancelled for the interior points (but not for points on element edges). However for a quadrilateral element or polygonal element, the areas of smoothing cells may not necessarily be equal, and they cannot be cancelled in general.

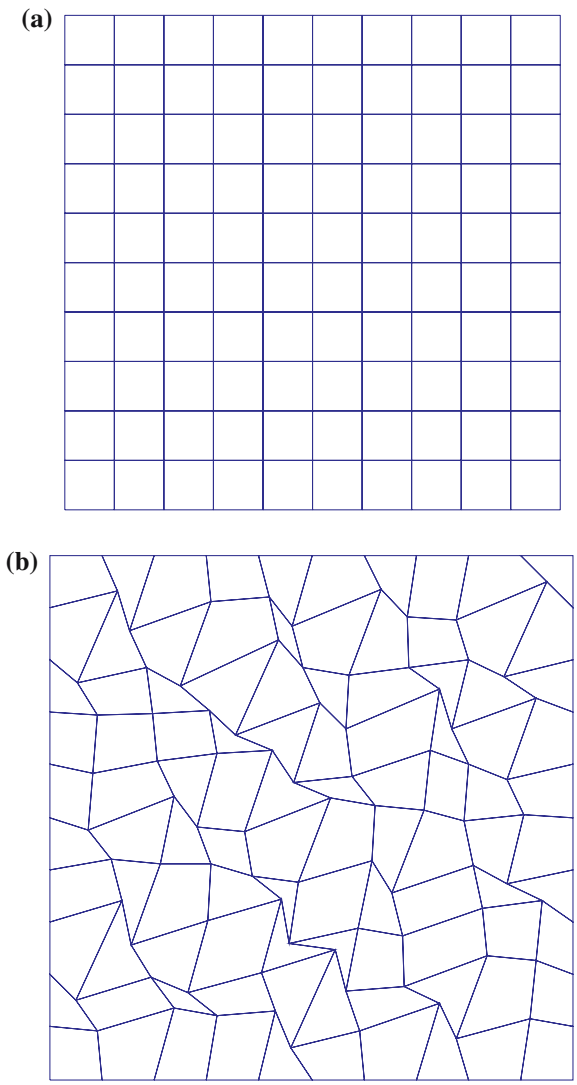

Fig. 6 Domain discretization using four-node elements. **a** Regular elements; **b** irregular elements

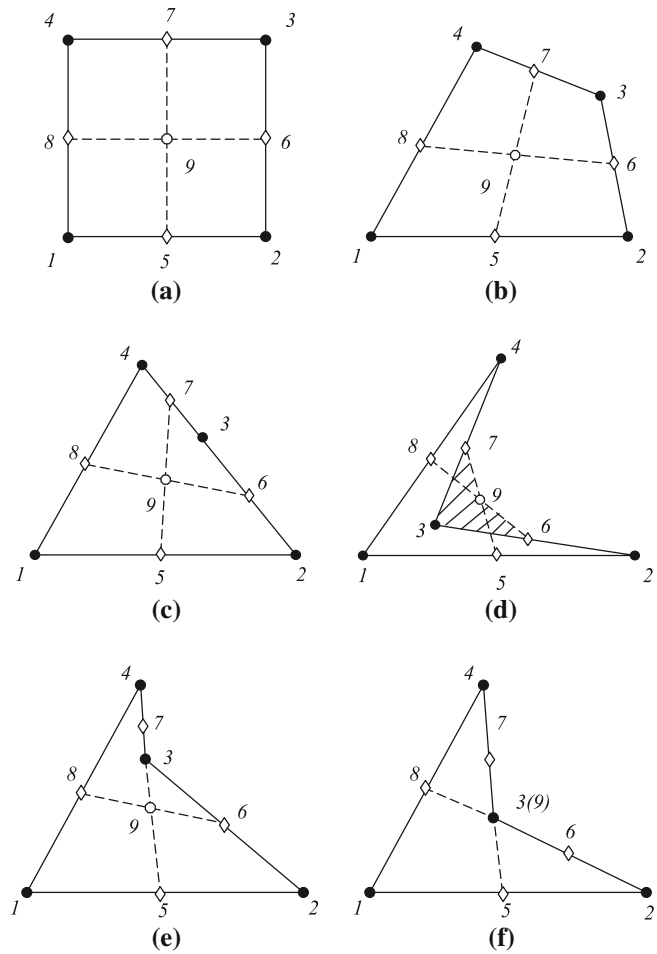

Fig. 7 A four-node element divided into four smoothing cells

To sum up, similar to the FEM, the SFEM shape functions should possess the following properties: (1) Delta function: $N_i(\mathbf{x}_j) = \delta_{ij}$; (2) Partition of unity: $\sum_{i=1}^{n} N_i(\mathbf{x}) = 1$; (3) Linear compatibility: $\sum_{i=1}^{n} N_i(\mathbf{x})\mathbf{x}_i = \mathbf{x}$; (4) $N_i(\mathbf{x}) \geq 0$. Any shape functions satisfying the four conditions can be used in SFEM.

4 Numerical implementation

4.1 Stability condition

To investigate the property of the proposed SFEM, an intensive numerical study has been conducted. SFEM results are compared with the conventional FEM using four-node isoparametric elements. Line integration is used for SFEM while domain (element) integration is used for FEM, and all the integrations are carried out using Gauss quadrature. First, we conduct the free vibration analysis of a free single element using the singular value decomposition technique. In SFEM, we first use an entire element as one smoothing cell (SC = 1) and plot the eigenmodes in Fig. 3a. Five spurious zero-energy modes are found, which do not carry proper deformation information. The smoothed integration cannot suppress the well-know hourglass modes. This means that the use of smoothed integration can still give rise to instabilities. We also found that FEM using only one Gauss point (GP = 1) gives identical eigenmodes as in Fig. 3a. Next we subdivide the element into four cells (SC = 4) and compare the results with those of FEM using 2×2 Gauss points (GP = 4). Once again the modes of the two methods coincide with each other. The corresponding eigenvalues are listed in Tables 2, 3, 4. From Fig. 3b, it is seen that, except three rigid-body-movement modes, no zero-energy modes exist in them, just as the FEM does using 2×2 Gauss points. In this case the solution will be stable. So far it can be concluded that the one-cell integration is "reduced" integration and the use of four cells can catch all the "deformed" modes properly in SFEM. Further comparison study is conducted using a single element

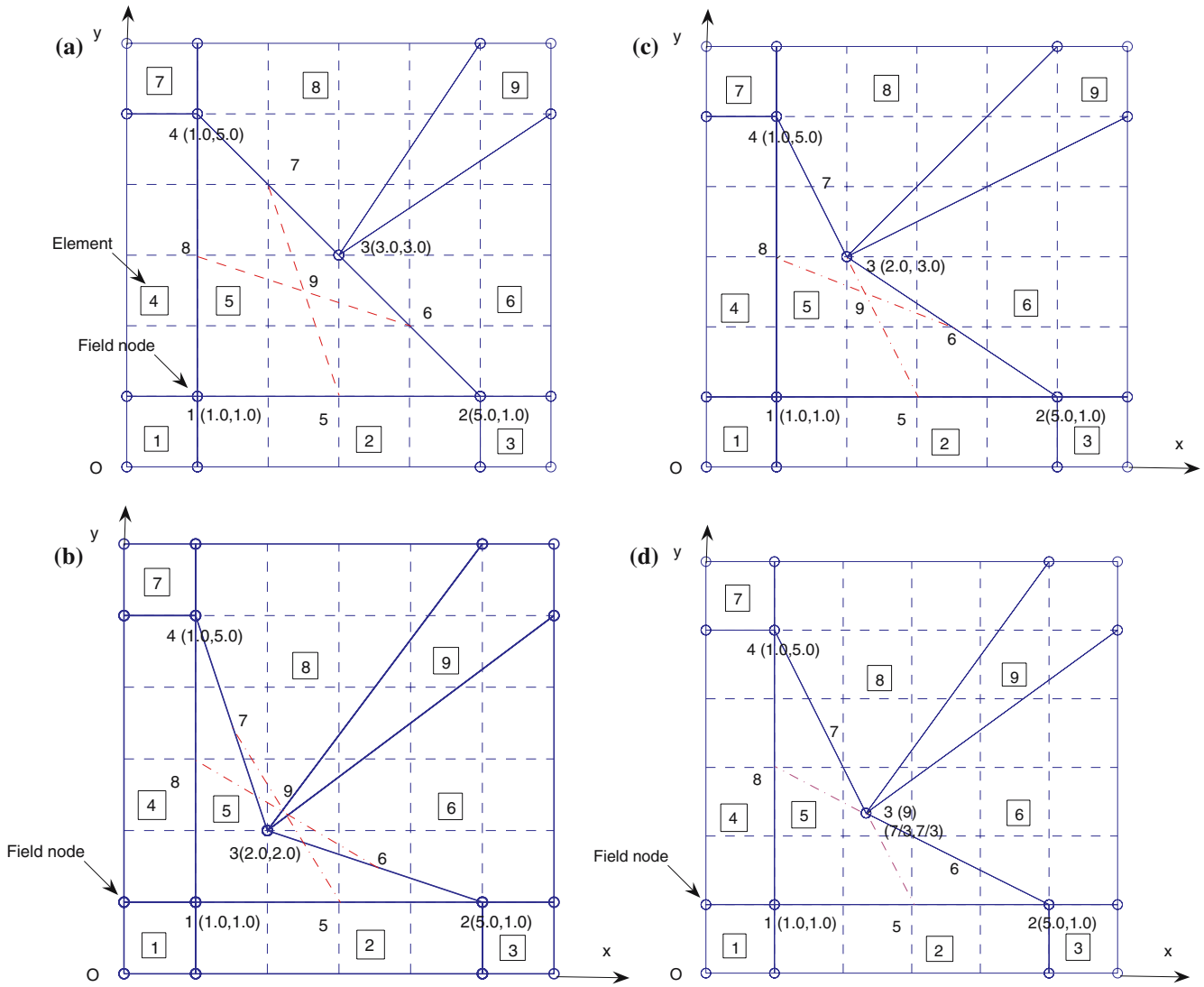

Fig. 8 Nodal arrangement of a solid using nine elements in patch test

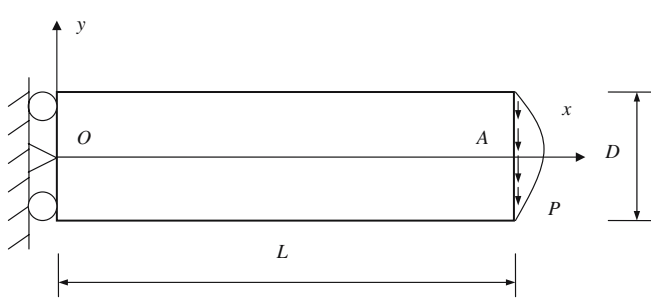

Fig. 9 Cantilever beam

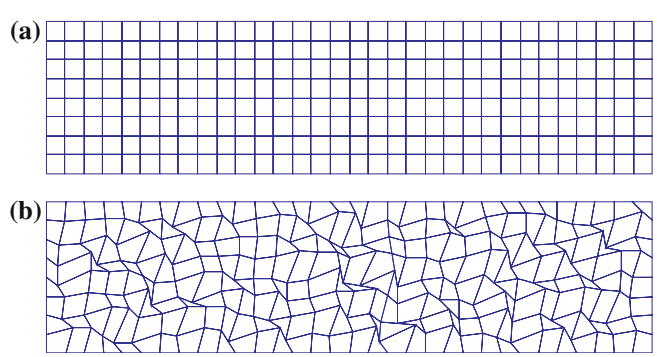

Fig. 10 Domain discretization of a beam using 4-node elements. **a** Regular elements; **b** extremely irregular elements

with three degrees-of-freedom (DOFs) fixed, and the same conclusion can be confirmed. The first eight eigenmodes corresponding to meshes using 4×4 elements are given in Fig. 4, from which the spurious zero-energy mode, rigid-body-movement mode and properly deformed mode can be clearly identified.

Division of a quadrilateral element into two or four triangular smoothing cells is also investigated as shown in Fig. 5.

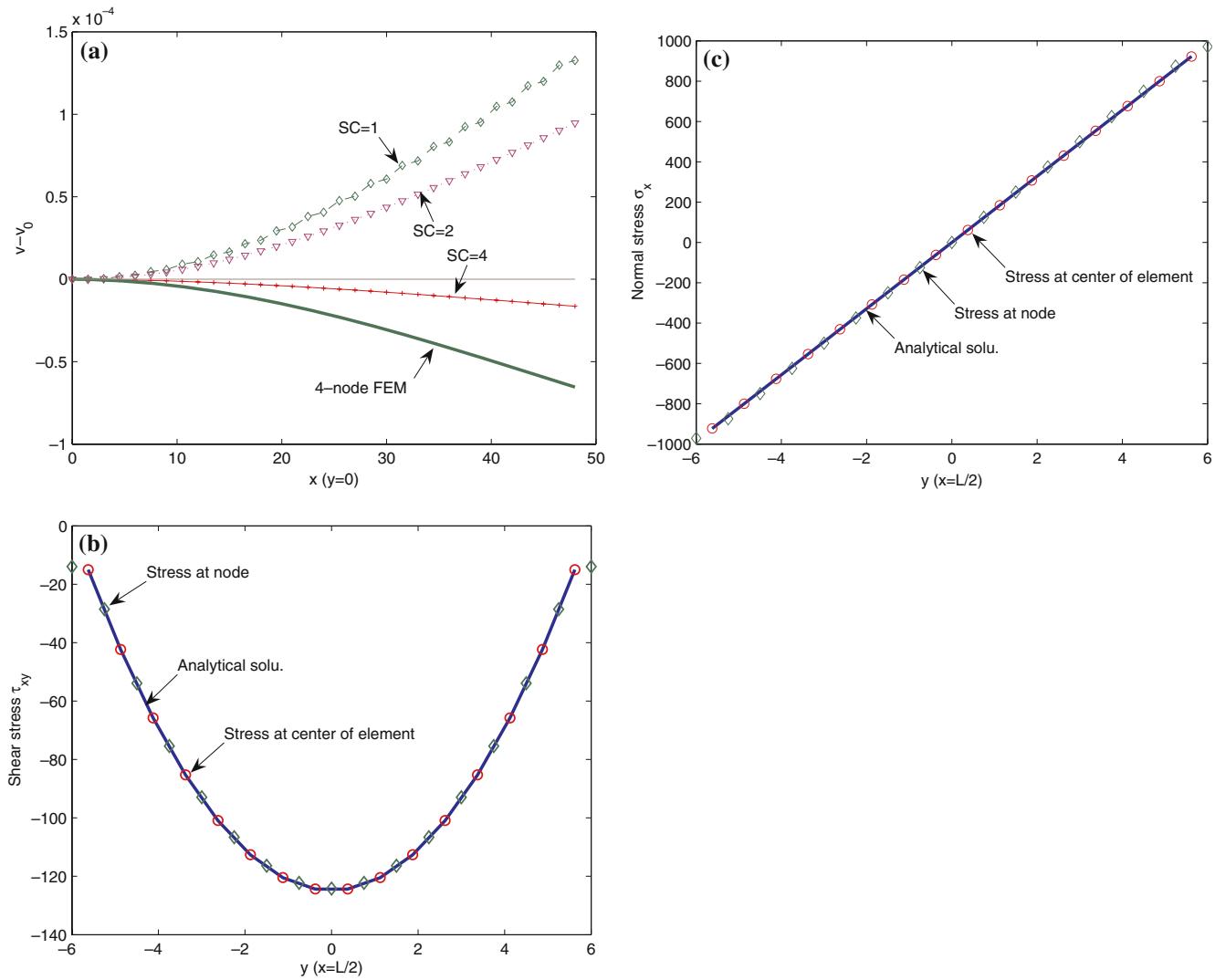

Fig. 11 Comparison of the numerical results of SFEM and analytical solutions. **a** Relative error in displacement v; **b** shear stress τ_{xy}; **c** normal stress σ_x

It is found that two triangular cells cannot suppress the zero-energy modes mentioned above. The eigenmodes of the four-triangular-SC case are the same as those obtained by four-quadrilateral-SC case. Due to the convenient post-processing of derivative variables, only four-quadrilateral SCs are used in the following examples. For a polygonal/tile element, we simply divide it into n triangular smoothing cells and accurate integration can be obtained, which is demonstrated in Fig. 5.

4.2 Procedure of SFEM

The numerical procedure for SFEM is briefed as follows.

1. Divide the domain into a set of elements and obtain information on node coordinates and element connectivity;
2. Loop over all the elements:
3. Loop over smoothing cells belonging to i-th element;
   a. Determine the area and outward unit normal of each side for cell Ω_C;
   b. Compute the $\tilde{\mathbf{B}}_C$ matrix using Eq. (12);
   c. Evaluate the stiffness matrix and force vector of the current cell;
   d. Assemble the contribution of the current cell to form element matrices and vectors using Eq. (14).
4. Implement essential boundary conditions;

Table 5 Tip displacements ($\times 10^{-3}$) of the cantilever beam using different regular elements (Analytical solu. = 8.900×10^{-3})

SC	8×2	16×4	32×8	64×16	128×32
1	11.617	9.436	9.031	8.937	8.908
2	10.602	9.262	8.990	8.926	8.906
4	8.551	8.800	8.884	8.896	8.899
FEM (GP=4)	7.969	8.644	8.884	8.884	8.896

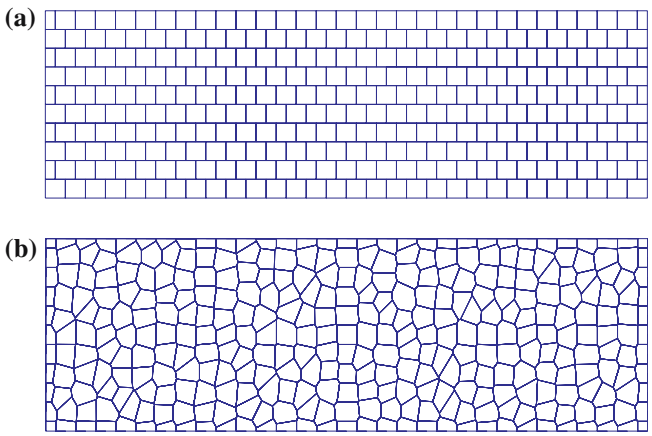

Fig. 12 Domain discretization of a beam using **a** tile elements and **b** Polygonal elements

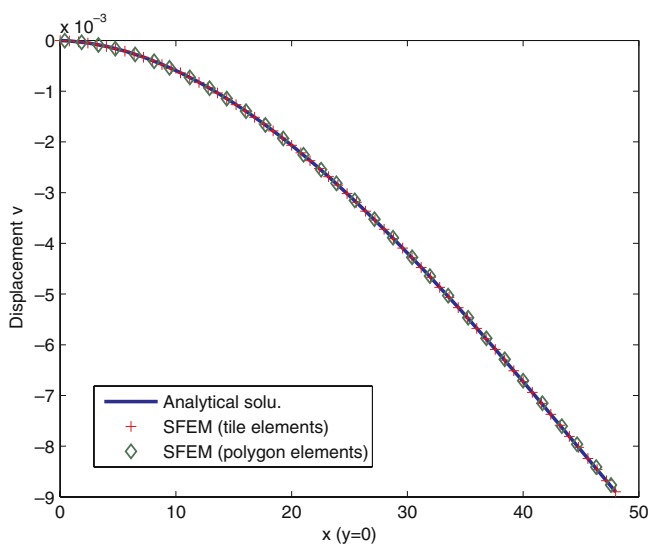

Fig. 13 Comparison of the numerical results of SFEM and analytical solutions using tile and polygonal elements

5. Solve the system equations to obtain the nodal displacements;
6. Evaluate strains and stresses at interested nodes.

It can be seen that the procedure of SFEM is in great similarity to that of conventional FEM except the computation of strain matrix. Compared with the conventional isoparametric finite element method, the present method possesses the following special features.

1. Shape functions in SFEM are more easily evaluated. They are practically obtained explicitly.
2. Field gradient is computed directly using shape functions. No derivative of shape functions is needed and thus the requirement on the smoothness of shape functions may be further relaxed.
3. No coordinate transformation or mapping is performed and the integration over the element becomes line integration on edges of smoothing cells. Therefore no restriction is imposed on the shape of element. Highly distorted element is allowed to use.

4.3 Standard patch test

A patch test is a sufficient requirement as a means of assessing the convergence of a numerical method based on Galerkin weak form. Linear displacements are imposed along the boundaries of a square patch with at least one interior node. Satisfaction of the patch test requires that the displacements of all the interior nodes follow "exactly" (to machine precision) the same function of the imposed displacement. Two types of discretization are used, as shown in Fig. 6: one with 10×10 regular elements and the other with irregular interior nodes whose coordinates are generated in the flowing fashion

$$\begin{aligned} x' &= x + \Delta x \cdot r_c \cdot \alpha_{ir} \\ y' &= y + \Delta y \cdot r_c \cdot \alpha_{ir}, \end{aligned} \tag{23}$$

where Δx and Δy are initial regular element sizes in x- and y-directions, respectively. r_c is a computer-generated random number between -1.0 and 1.0 and α_{ir} is a prescribed irregularity factor whose value is chosen between 0.0 and 0.5. The bigger the value of α_{ir}, the more irregular the shape of generated elements. The following error norm in displacement is used to examine the computed results.

$$e_d = \frac{\sum_{i=1}^{ndof} \left| u_i - u_i^h \right|}{\sum_{i=1}^{ndof} \left| u_i \right|}. \tag{24}$$

Here ndof is the total number of DOFs in the problem. It is found that the SFEM can pass the patch test within machine precision regardless of the number of SC and α_{ir} used.

As mentioned above, no mapping or coordinate transformation is required and thus no Jacobian matrix and its inverse are evaluated in the SFEM. The method is valid for very irregular elements. Some commonly encountered cases are demonstrated in Fig. 7, in which (a) and (b) are normal and desired cases in FEM while (c)–(f) are usually prohibited. Three nodes are collinear in (c) while in (d) the intersection point #9 of two bimedians is located outside the element region. In (e) node #3 is on the bimedian joining the midpoints 5 and 7 and in (f) point #9 coincides exactly with node #3. The feature of the last four can be expressed as

$$\max(\alpha_i) \geq \pi, \quad (i = 1, 2, 3, 4), \tag{25}$$

where α_i is the interior angle of a quadrilateral element.

The patches with elements of extremely irregular shapes, as demonstrated in Fig. 8 correspond to the last four cases in Fig. 7. Standard patch test is conducted for all the cases in Fig. 8. As expected, all the patches can pass the standard patch test within machine precision. In case (b), the cell 96379 is automatically sequenced reversely as compared to other cases and outside unit normal becomes inside unit normal and hence above formulations are still valid. It should be mentioned that, in case (d), as point #9 coincides with the

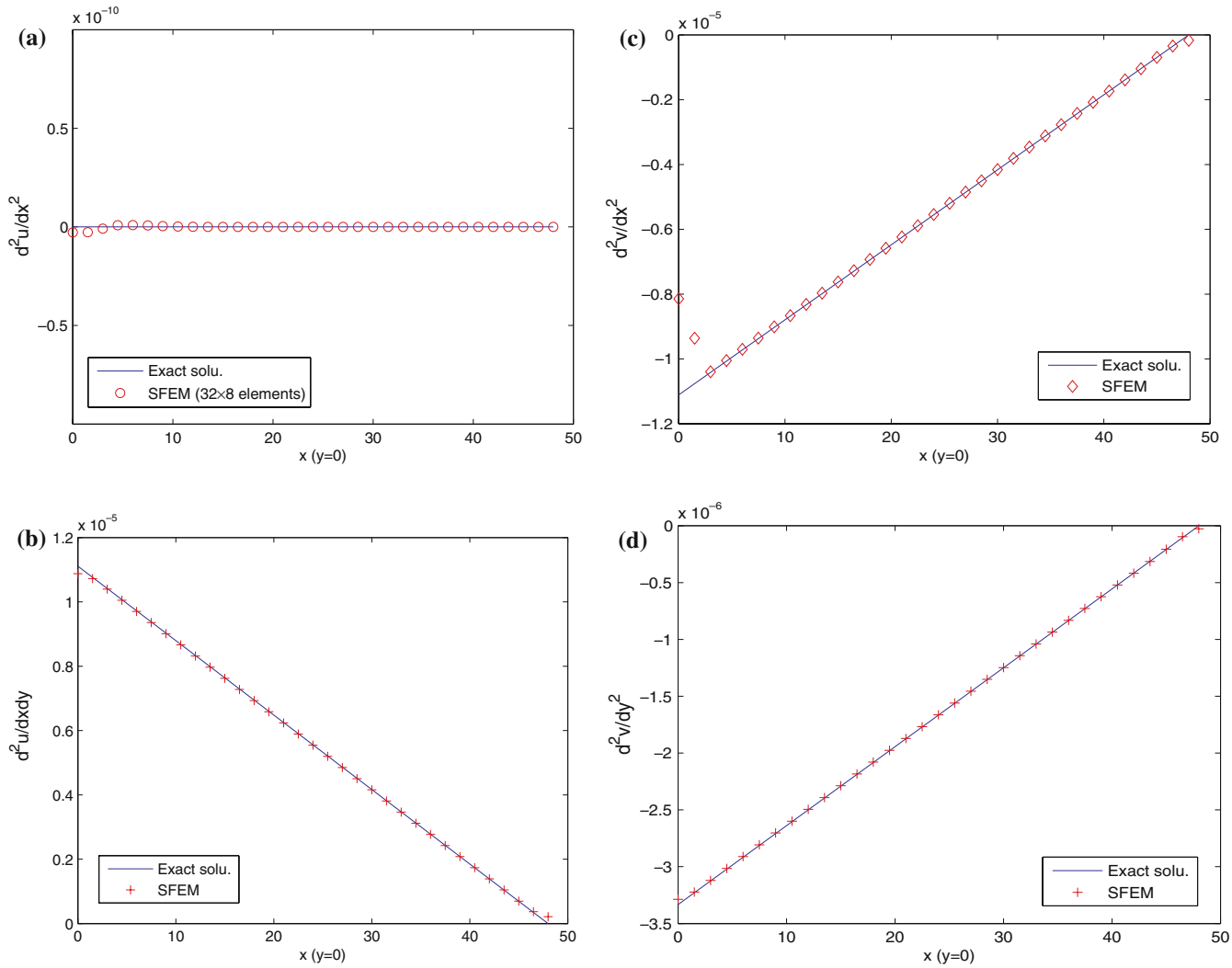

Fig. 14 Second order displacement gradients. **a** $\partial^2 u/\partial x^2$; **b** $\partial^2 u/\partial x \partial y$; **c** $\partial^2 v/\partial x^2$; **d** $\partial^2 v/\partial y^2$

element node #3, it should accordingly adopt the same shape function values as this node.

In comparison, the shape of quadrilateral element in FEM cannot be severely distorted and any interior angle of a quadrilateral element should be less than 180° in theory and 120° in practice. Therefore the last four cases should always be avoided as their determinants of the Jacobian matrix are zero or negative. However, in the proposed SFEM, such a limit is not necessary. The effect of irregularity factor on solution accuracy will be discussed through the following numerical examples.

5 Numerical examples

5.1 Cantilever beam

A cantilever beam with length L and height D is studied as benchmark problem here, which is subjected to a parabolic traction at the free end as shown in Fig. 9. The beam is assumed to have a unit thickness so that plane stress condition is valid. The analytical solution is available and can be found in a textbook by Timoshenko and Goodier [21].

$$\begin{aligned} u_1 &= \frac{Py}{6EI}\left[(6L-3x)x+(2+v)(y^2-\frac{D^2}{4})\right] \\ u_2 &= -\frac{P}{6EI}\left[3vy^2(L-x)+(4+5v)\frac{D^2x}{4}+(3L-x)x^2\right], \end{aligned} \tag{26}$$

where the moment of inertia I of the beam is given by $I = D^3/12$.

The stresses corresponding to the displacements Eq. (26) are

$$\begin{aligned} \sigma_{11}(x,y) &= \frac{P(L-x)y}{I} \\ \sigma_{22}(x,y) &= 0 \\ \tau_{12}(x,y) &= -\frac{P}{2I}\left(\frac{D^2}{4}-y^2\right) \end{aligned} \tag{27}$$

The related parameters are taken as $E = 3.0 \times 10^7$ kPa, $v = 0.3$, $D = 12$ m, $L = 48$ m and $P = 1{,}000$ N.

In order to study the convergence rate of the present method, two norms are used here, i.e., displacement norm

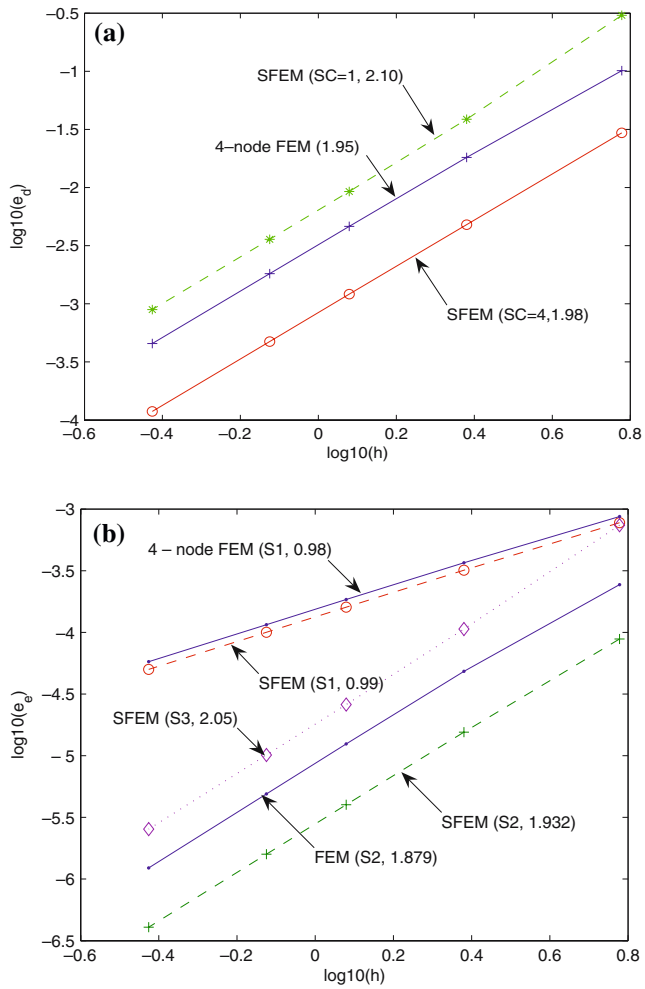

Fig. 15 Comparison of convergence rate between SFEM and FEM. **a** Displacement norm; **b** energy norm. Note that in Scheme 1 (S1), SC/GP=4 is employed for calculation of both stiffness matrix (displacement) and stresses (energy) while in Scheme 2 (S2), SC/GP=4 is used only for calculation of stiffness matrix (displacement), and SC/GP=1 is used for post-processing of stresses and energy. In Scheme 3 (S3), SC/GP=1 is used all the time

Table 6 Relative errors of the cantilever beam using different element sizes (regular elements, SFEM: SC = 4, FEM: GP = 4)

Elements		20×5	32×8	40×10	64×16	128×32
Δh		2.4	1.5	1.2	0.75	0.375
Δe_d	SFEM	4.789e-3	1.886e-3	1.210e-3	4.741e-4	1.188e-4
	FEM	1.816e-2	7.204e-3	4.628e-3	1.816e-3	4.551e-4
Δe_e	SFEM	3.189e-4	1.999e-4	1.600e-4	1.001e-4	5.007e-5
	FEM	3.663e-4	2.304e-4	1.846e-4	1.155e-4	5.781e-5
CPU time (s)	SFEM	0.625	1.110	1.766	4.594	31.083
	FEM	0.562	1.110	1.656	4.532	36.127

and energy norm. The displacement norm is given in Eq. (24) and the energy norm is defined by

$$e_e = \frac{1}{2LD}\left[\int_\Omega (\varepsilon^h - \varepsilon)^{\mathrm{T}}\mathbf{D}(\varepsilon^h - \varepsilon)\right]^{1/2}. \tag{28}$$

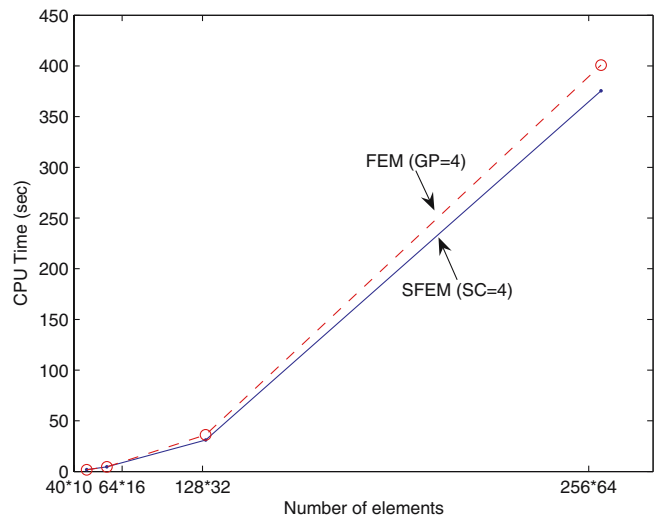

Fig. 16 Comparison of CPU time between FEM and SFEM (exclusive of solving algebraic equations)

Table 7 Relative errors of the cantilever beam using irregular elements (40×10 elements)

α_{ir}	FEM (4 GPs)		SFEM (SC = 4)			
	Δe_d	Δe_e	Δe_d^{a}	Δe_e^{a}	Δe_e^{a}	Δe_e^{a}
0.1	4.925e-3	1.904e-4	1.455e-3	(1.334e-3)	1.656e-4	(1.658e-4)
0.2	6.028e-3	2.099e-4	2.509e-3	(2.086e-3)	1.843e-4	(1.854e-4)
0.3	7.673e-3	2.310e-4	3.808e-3	(2.612e-3)	2.033e-4	(2.060e-4)
0.4	1.024e-2	2.692e-4	5.880e-3	(4.545e-3)	2.379e-4	(2.493e-4)
0.5	Fail	Fail	9.118e-3	(7.973e-3)	2.855e-4	(3.553e-4)
0.0 (regular)	4.628e-3	1.846e-4	1.210e-3	(1.210e-3)	1.600e-4	(1.600e-4)

[a] Results in parentheses correspond to the case that shape functions at point #9 are evaluated using Eq. (22)

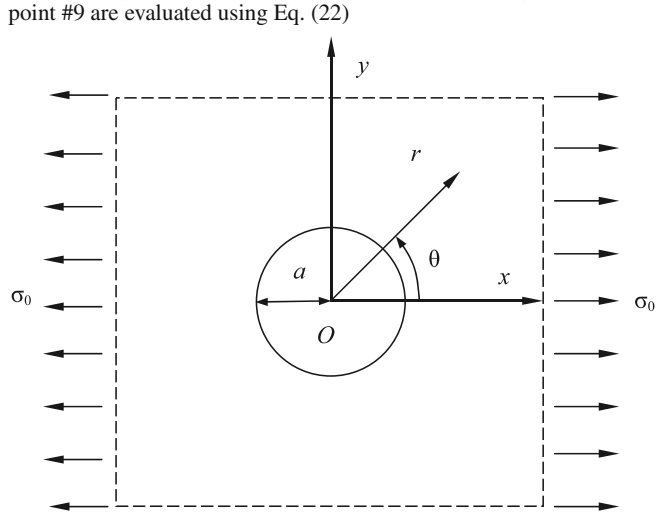

Fig. 17 Infinite plate with a circular hole subjected to unidirectional tension

In the computations, the nodes on the left boundary are constrained using the exact displacements obtained from Eq. (26) and the loading on the right boundary uses the distributed parabolic shear stresses in Eq. (27). The beam is analyzed using different number of elements and smoothing cells. Figure 10 gives one example for the discretization.

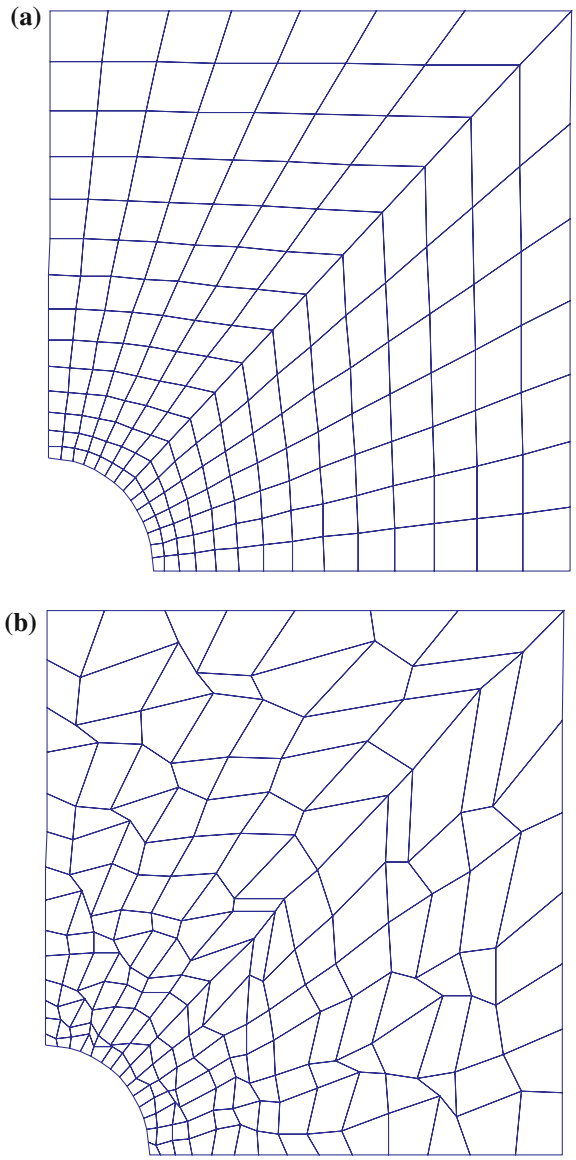

Fig. 18 Domain discretization of the infinite plate with a hole using four-node element. **a** Regular elements; **b** Extremely irregular elements

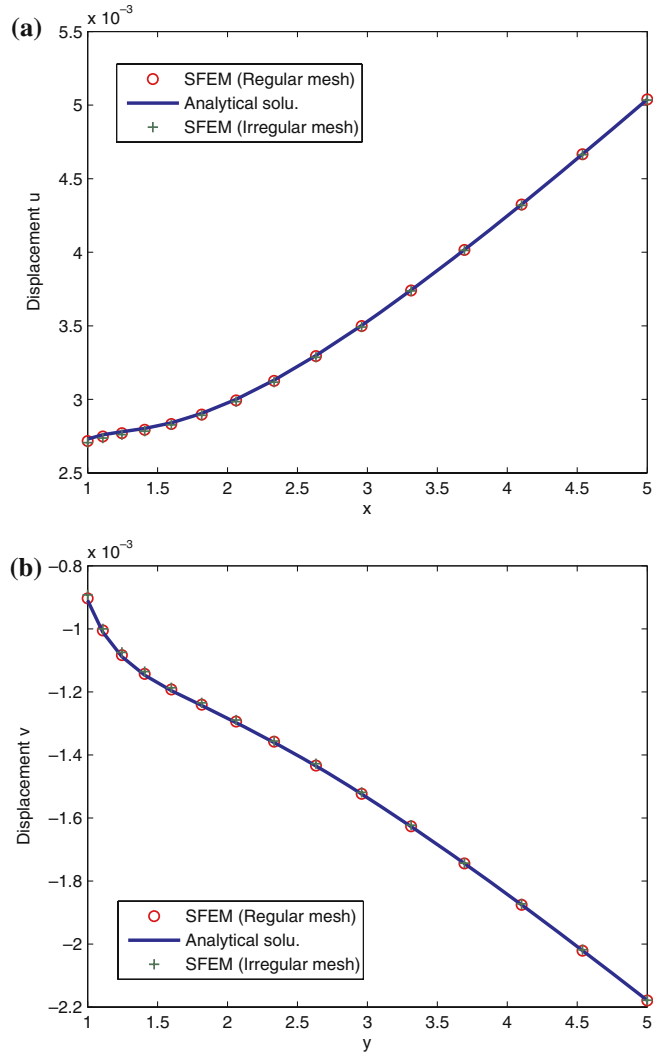

Fig. 19 Computed and exact displacements of the infinite plate with a hole. **a** u; **b** v

When SC = 2, the element is divided only in x-directions. From the results in Table 5, it is seen that, if an entire element is selected as one smoothing patch (SC = 1), the displacement is always overestimated as compared to the analytical solution the solution corresponds to equilibrium model (upper bound solution), which is responsible for the over-predicted displacements. Though the spurious mode does not appear in this setting, the under-integration gives relatively low accuracy. If an element is divided into four smoothing cells (SC = 4) or more, the computed displacement is smaller than the exact one, but more accurate than that of FEM based on pure displacement compatible formulation, which is the lower bound solution. The computed deflection and the shear stress are shown in Fig. 11. The numerical results agree well with the analytical solutions. From Fig. 11a, it is observed that, with the increase of the number of SC, the SFEM results approach FEM gradually, though the latter may not necessarily be more accurate. There exists an optimal value of SC that gives the best results as compared to the exact ones.

When computing stresses using 4SC, we can average four sets of stresses related to each smoothing cell and regard them as those of this element. The stress can be weighted using the respective area of each cell. Similarly, to calculate stresses at a node, we simply average the stresses of four cells associated with this nodes. It is seen from Fig. 11b that both methods give very good approximation of stresses. To demonstrate the capability of the SFEM with elements of complex shapes, the beam is divided into tile elements and polygonal elements, as shown in Fig. 12. The deflections are then compared and plotted together with exact solutions in Fig. 13. Once again the numerical results are in good accord as compared with exact ones. Note clearly that these types of elements cannot be used in the conventional FEM.

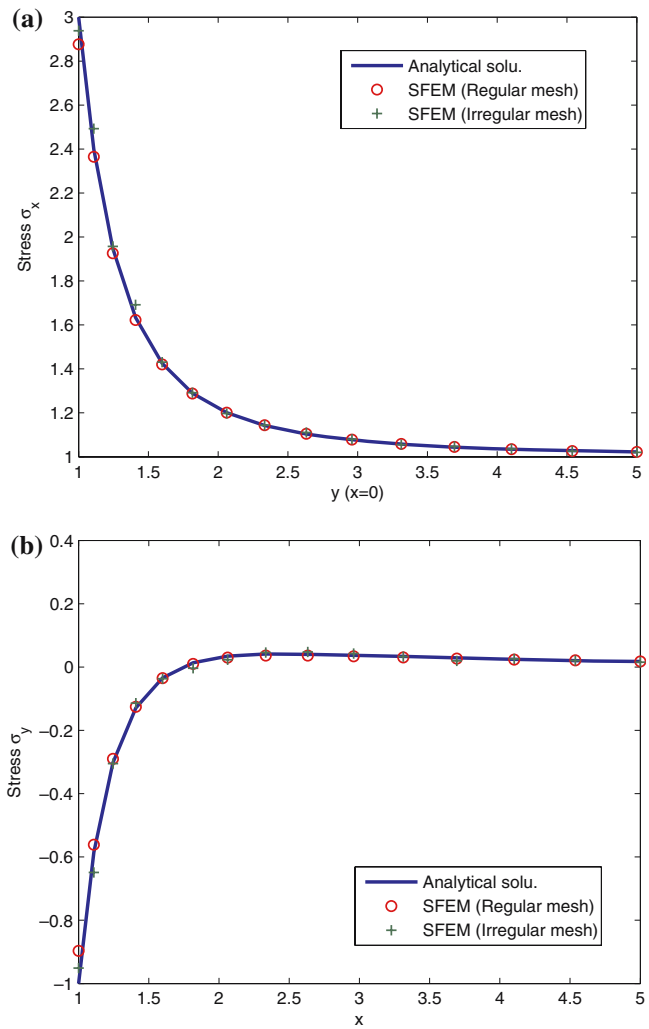

Fig. 20 Computed and exact stresses of the infinite plate with a hole. **a** σ_x; **b** σ_y

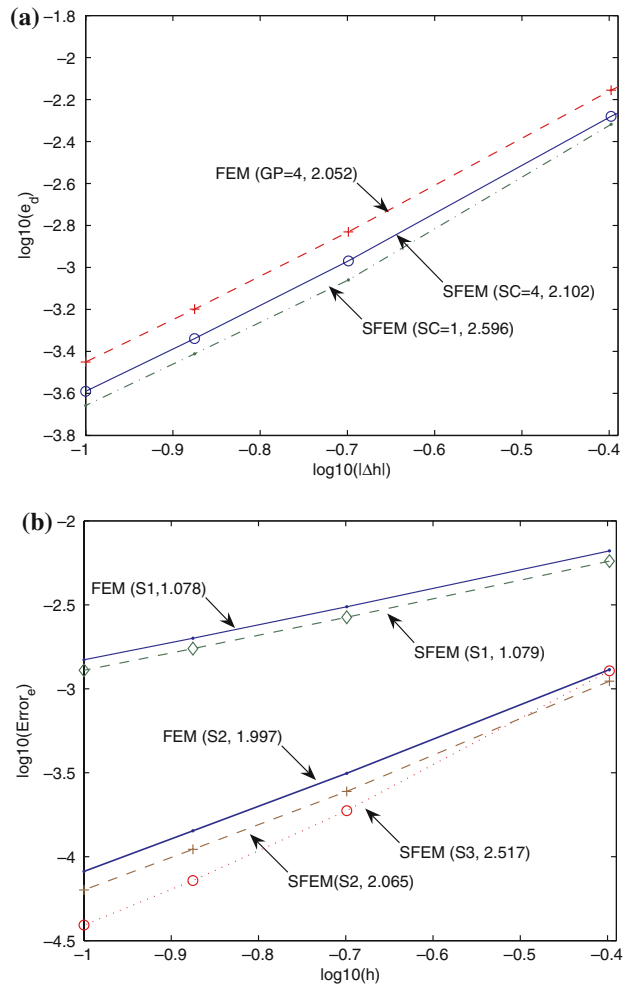

Fig. 21 Comparison of convergence rate between SFEM and FEM. **a** Displacement norm; **b** Energy norm

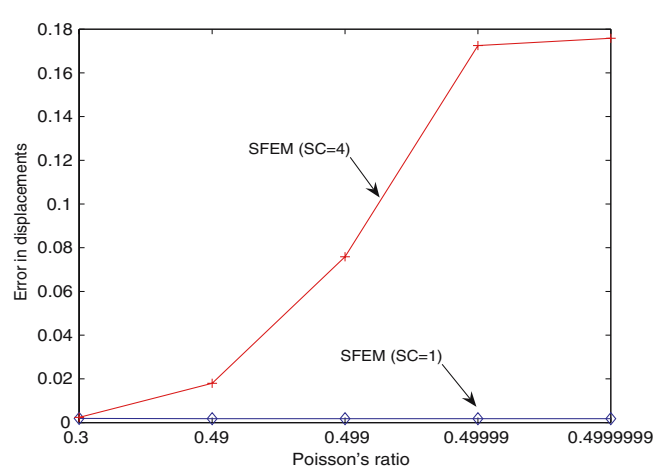

Fig. 22 Error in displacement using various Poisson's ratios

Figure 14 illustrates the second-order displacement gradients obtained using SFEM and the equations suggested in Sect. 2. The SFEM results are in good agreement with the analytical solutions. The gradients near the boundaries are generally less accurate when compared with the internal region because those nodes are unlikely to be the points of optimal accuracy for gradients. This phenomenon is also reported in nodal–natural element method [23].

The relative errors in displacement and energy of SFEM are compared with four-node bilinear finite elements in Table 6. The convergence rates are also demonstrated in Fig. 15 using two schemes for energy calculation (S1 and S2). It is seen that both methods achieve the equivalent convergence rates in displacement and energy while the displacement of SFEM is more accurate than FEM. The energy of SFEM using S2 converges about one time faster as compared to that using S1. When comparing the computational cost in Fig. 16, we can see that both methods require nearly the same CPU time when number of elements is not very large. With the increase of elements, however, it appears that FEM takes more CPU time than SFEM.

To investigate the effect of element irregularity factor, we perform the same analysis with enlarged α_{ir} (See Fig. 10).

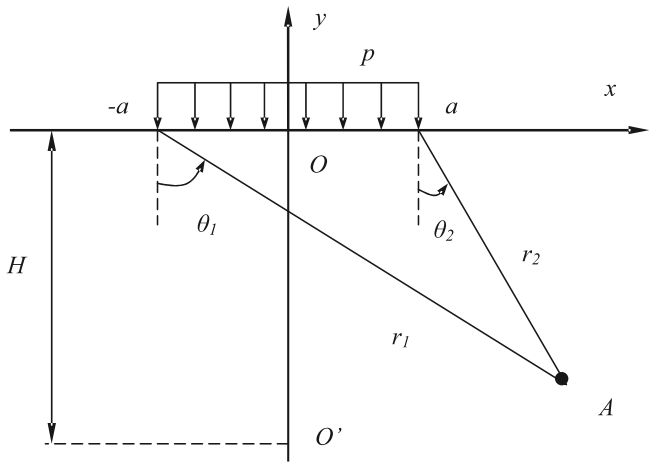

Fig. 23 Semi-infinite plane subjected to a uniform pressure

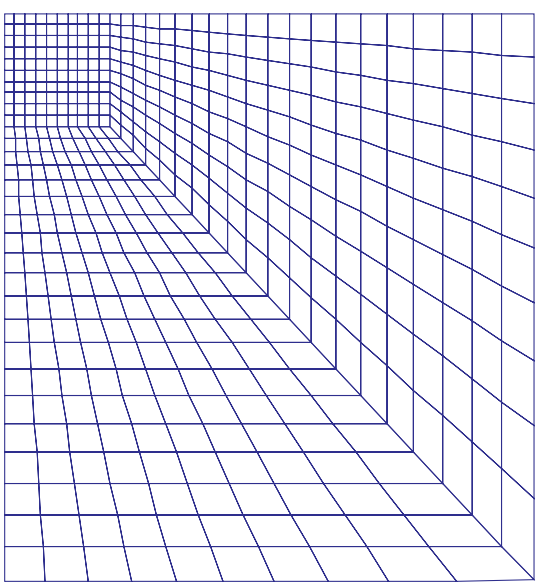

Fig. 24 Domain discretization of the semi-infinite plane using four-node elements

From Table 7, it is noticed once again that SFEM is always more accurate than FEM both in displacement and energy when using the same meshes. When the shape of element is severely distorted, FEM may fail to work due to the negative determinant of Jacobian matrix. Compared with regular element, irregular meshes degrade the accuracy of computed results for both methods. The more irregular the shape of elements, the less accurate the numerical results. The errors in the parentheses are obtained using shape functions at point #9 evaluated from Eq. (22). It is seen that the accuracy of displacement is improved but the energy is degraded especially for very irregular meshes.

5.2 Infinite plate with a circular hole

Figure 17 represents a plate with a central circular hole subjected to a unidirectional tensile load of 1.0 N/m at infinity

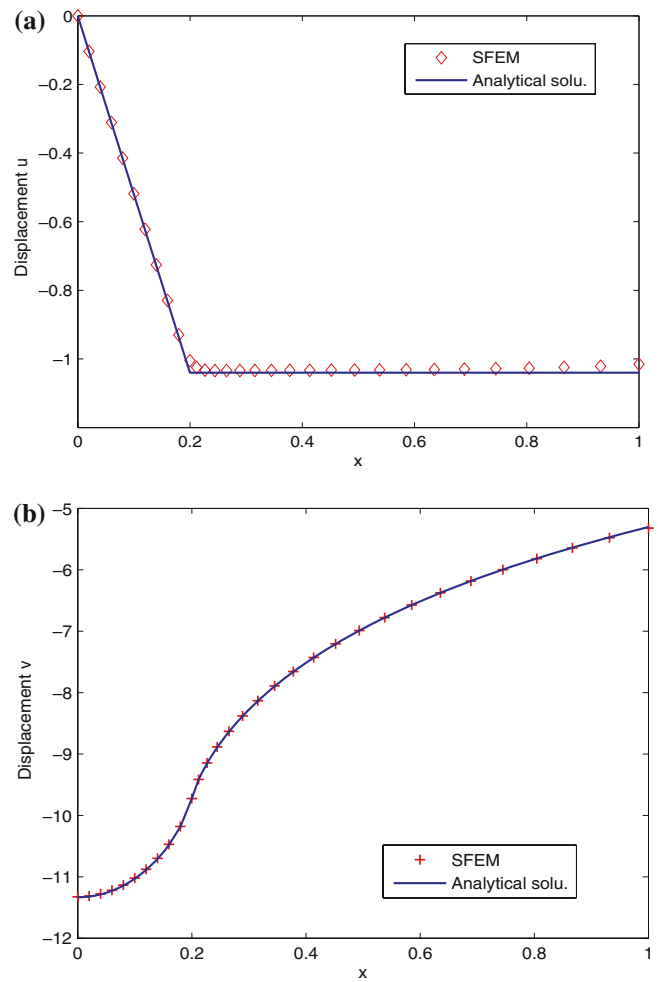

Fig. 25 Computed and exact displacements of the semi-infinite plane. **a** u; **b** v

in the x -direction and Fig. 18 gives the discretization of the domain using four-node elements. Due to its symmetry, only the upper right quadrant of the plate is modeled. Plane strain condition is considered and $E = 1.0 \times 10^3\,\mathrm{N/m^2}$, $\upsilon = 0.3$. Symmetry conditions are imposed on the left and bottom edges, and the inner boundary of the hole is traction free. The exact solution for the stresses is ([21])

$$\begin{aligned}
\sigma_{11} &= 1 - \tfrac{a^2}{r^2}\left[\tfrac{3}{2}\cos 2\theta + \cos 4\theta\right] + \tfrac{3a^4}{2r^4}\cos 4\theta \\
\sigma_{22} &= -\tfrac{a^2}{r^2}\left[\tfrac{1}{2}\cos 2\theta - \cos 4\theta\right] - \tfrac{3a^4}{2r^4}\cos 4\theta, \\
\tau_{12} &= -\tfrac{a^2}{r^2}\left[\tfrac{1}{2}\sin 2\theta + \sin 4\theta\right] + \tfrac{3a^4}{2r^4}\sin 4\theta
\end{aligned} \tag{29}$$

where (r, θ) are the polar coordinates and θ is measured counterclockwise from the positive x-axis. Traction boundary conditions are imposed on the right ($x = 5$) and top ($y = 5$) edges based on the exact solution Eq. (29). The displacement components corresponding to the stresses are

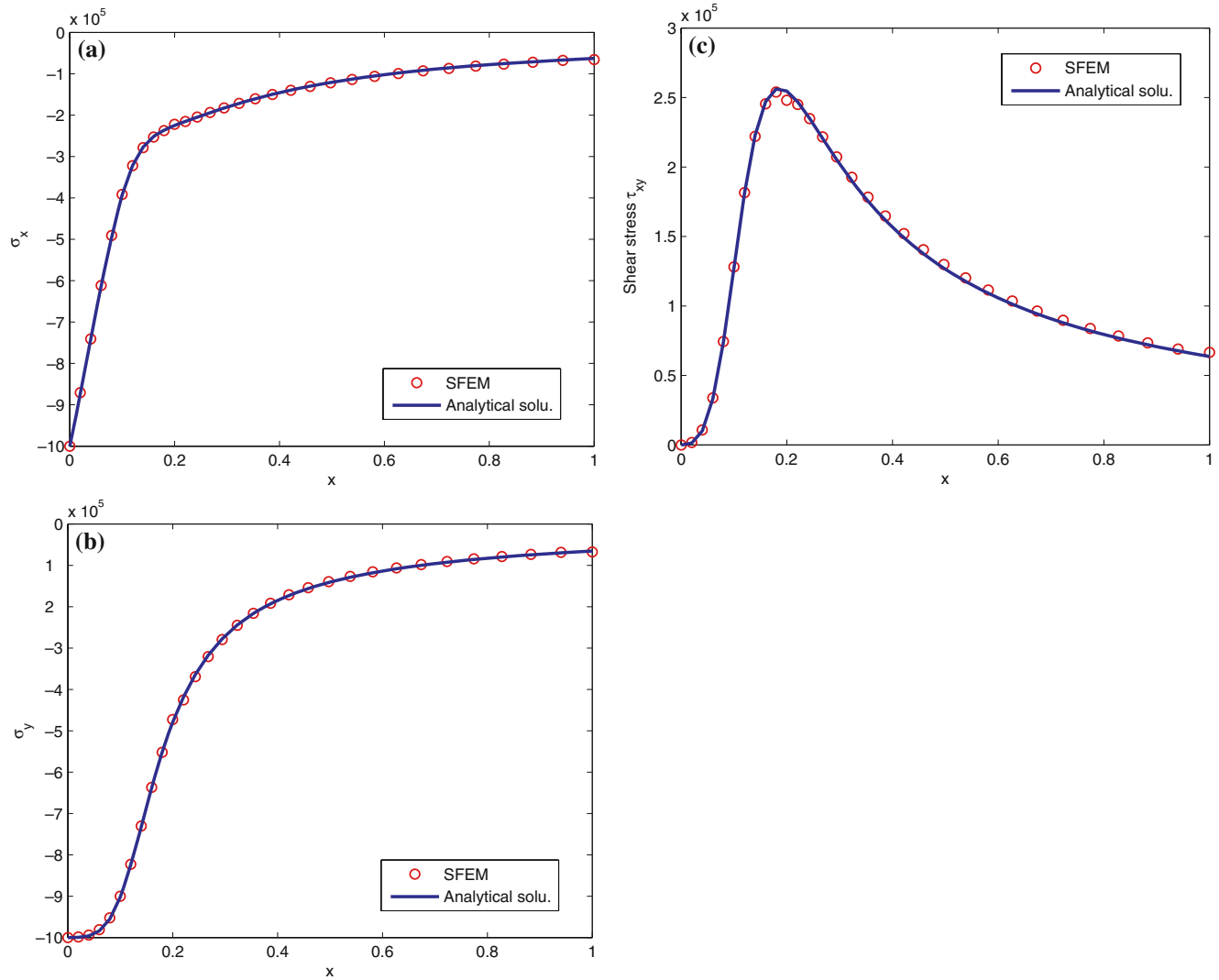

Fig. 26 Computed and exact stresses of the semi-infinite plane. **a** σ_x; **b** σ_y; **c** τ_{xy}

$$u_1 = \frac{a}{8\mu}\left[\frac{r}{a}(\kappa+1)\cos\theta+2\frac{a}{r}\left((1+\kappa)\cos\theta+\cos 3\theta\right)-2\frac{a^3}{r^3}\cos 3\theta\right]$$
$$u_2 = \frac{a}{8\mu}\left[\frac{r}{a}(\kappa-1)\sin\theta+2\frac{a}{r}\left((1-\kappa)\sin\theta+\sin 3\theta\right)-2\frac{a^3}{r^3}\sin 3\theta\right], \tag{30}$$

where κ is defined in terms of Poisson's ratio by $\kappa = 3 - 4v$ for plane strain cases.

The domain is discretized using 196 regular and relatively irregular quadrilateral elements. Each element is divided into four smoothing cells. From Figs. 19 and 20, it is observed that all the computed displacements and stresses are in good agreement with the analytical solutions. Very irregular mesh still gives desired results. Note that triangular elements are also tested and it has been found that the results of both FEM and SFEM are identical, as expected. The convergence rates in displacement and energy are demonstrated in Fig. 21. It is observed that the energy rate of SFEM using S2 is still faster if compared to its counterpart of FEM, both of which achieve a comparable speed in displacement. For a very coarse mesh, the energy of SFEM is less accurate as compared to that of FEM. However, as the meshes are refined, it is much more accurate than of FEM.

To check the availability of SFEM in nearly incompressible material, we make the Poisson's ratio approach 0.5 gradually. It is found from Fig. 22, that the SFEM is not particularly better than the FEM based on displacement formulation for solving this kind of locking problems, which in addition demonstrate the difference of SFEM from the $\mathbf{u} - \boldsymbol{\varepsilon}$ mixed formulations in FEM.

5.3 Semi-infinite plane

A semi-infinite plane shown in Fig. 23 is studied subjected to a uniform pressure within a finite range ($-a \le x \le a$). Plane strain condition is considered. The analytical stresses

are given by

$$\sigma_{11} = \frac{p}{2\pi}[2(\theta_1 - \theta_2) - \sin 2\theta_1 + \sin 2\theta_2]$$
$$\sigma_{22} = \frac{p}{2\pi}[2(\theta_1 - \theta_2) + \sin 2\theta_1 - \sin 2\theta_2]. \quad (31)$$
$$\tau_{12} = \frac{p}{2\pi}[\cos 2\theta_1 - \cos 2\theta_2]$$

The directions of θ_1 and θ_2 are referred in the figure. The corresponding displacements can be expressed as

$$u_1 = \frac{p(1-v^2)}{\pi E}\left[\frac{1-2v}{1-v}\left[(x+a)\theta_1-(x-a)\theta_2\right]+2y\ln\frac{r_1}{r_2}\right]$$
$$u_2 = \frac{p(1-v^2)}{\pi E}\left[\begin{array}{l}\frac{1-2v}{1-v}\left[y\left(\theta_1-\theta_2\right)+2\mathrm{Harctan}\frac{1}{c}\right]+2(x-a)\ln r_2\\ -2(x+a)\ln r_1+4a\ln a+2a\ln\left(1+c^2\right)\end{array}\right] \quad (32)$$

where $H = ca$ is the distance from the origin to the point O' where the vertical displacement is assumed to be zero and c is a coefficient.

Due to the symmetry about y-axis, the problem is modeled with a 5 $a \times 5a$ square with $a = 0.2\,\mathrm{m}$, $c = 100$ and $p = 1\,\mathrm{MPa}$. The left and bottom sides are constrained using exact displacement in Eq. (32) while the right side is subjected to tractions computed from Eq. (31). The domain is discretized using 418 elements as shown in Fig. 24. Four smoothing cells are used for each element. The computed displacements along the free surface ($y = 0$) are demonstrated in Fig. 25 while the stress distributions along the diagonal line of the semi-infinite plane ($y = -x$) are given in Fig. 26. It is seen that all the numerical results using SFEM are in good accord with the analytical solutions. The convergence rates in displacement and energy defined in Eqs. (22) and (26) are also investigated and compared with four-node finite elements as shown in Fig. 27. Similar to the previous example, the displacement obtained from SFEM achieves the same convergence rate as FEM but the energy of the former converges faster than the latter. The SFEM results are more accurate than those of FEM when using Scheme 2 for energy calculation.

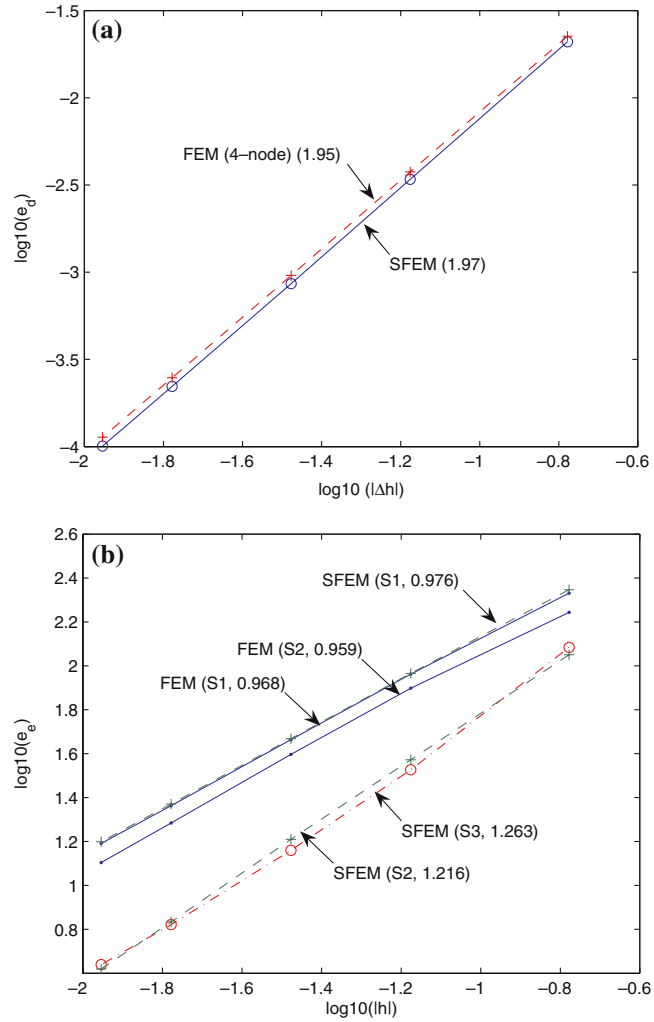

Fig. 27 Comparison of convergence rate between SFEM and FEM. **a** Displacement norm; **b** energy norm

5.4 High-gradient heat conduction problem

Finally, a heat conduction problem is considered in a rectangular plate (as shown in Fig. 28) with heat source

$$b(x, y) = 2s^2 \sec h^2[s(y-3)]\tanh[s(y-3)]. \quad (33)$$

The boundary conditions are given by

$$\begin{array}{l} T = -\tan\mathrm{h}(3s) \quad \text{at } y = 0 \\ T = \tan\mathrm{h}(3s) \quad \text{at } y = 6 \\ \frac{\partial T}{\partial x} = 0 \quad \text{at } x = -0.25 \text{ and } x = 0.25 \end{array} \quad (34)$$

The exact solution of this problem is

$$T = \tanh[s(y-3)]. \quad (35)$$

As shown in the study by Belytschko et al. [3] this problem has a very high gradient of temperature near $y = 3.0$. In Eq. (33), the quantity s is a free parameter. The bigger the value of s, the higher the gradient of field T. As the steep gradient occurs only near the area $2.5 \le y \le 3.5$. Relatively small (10×40) rectangular elements are used to discretize this area. For the other two parts, (10×25) rectangular elements are used, respectively. For comparison, the four-node isoparametric finite elements are applied to analyze this problem. Note that $s = 40$ is used in the analysis.

The distribution of computed temperature along y-axis is illustrated in Fig. 29, which once again compares well with the analytical ones. Then we increase the number of smoothing cells or Gauss points in FEM and study the relative error of temperature using Eq. (24). From the results listed in Table 8, we notice that, when GP/SC = 4, the temperature obtained by SFEM is much more accurate than that of FEM. Increase of GP/SC can enhance the accuracy for both methods when dealing with high gradient problems. Gauss integration converges much faster to exact solutions. When investigating the gradient of the temperature, we notice that the two methods give comparable results. Both computed results are not very accurate at the tip as compared with the exact ones. The linear

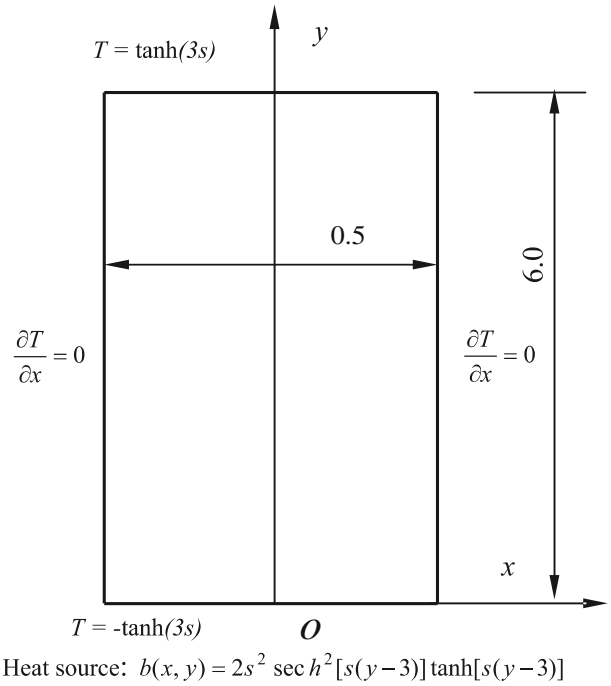

Fig. 28 Heat conduction in a rectangular plate

Table 8 Relative errors ($\times 10^{-5}$) in temperature of the heat-transfer problems using different Gauss points/Smoothing cells

GP/SC	FEM	SFEM
2×2	245.226	18.745
3×3	22.766	8.276
4×4	1.055	4.654

field approximation in both methods may be responsible for the inadequate accuracy of the field gradient.

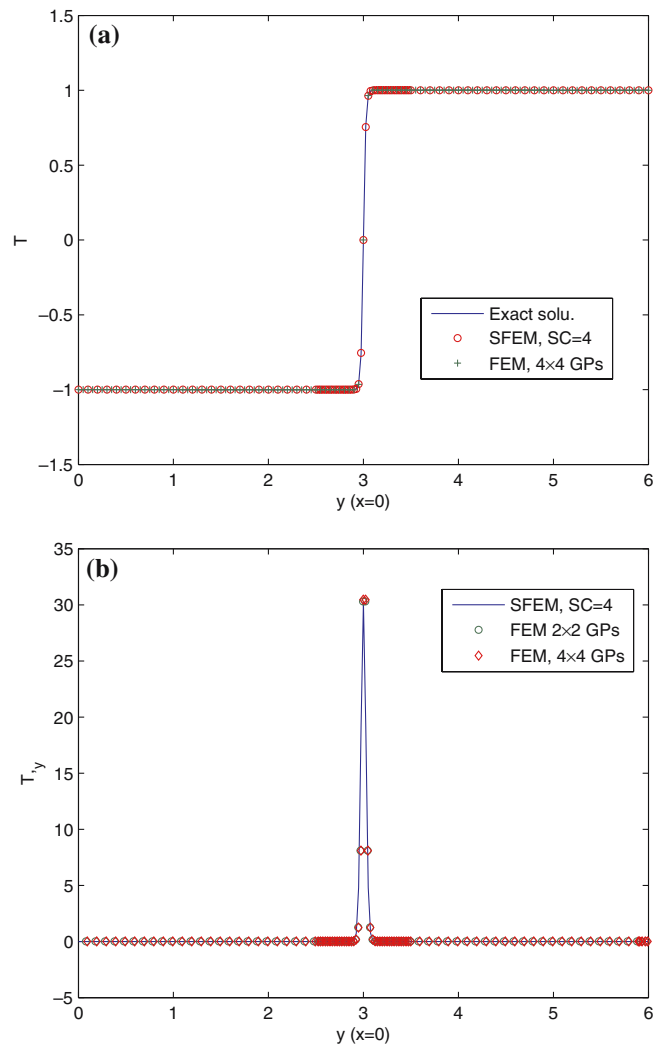

Fig. 29 Computed and exact solutions for the high-gradient problem. **a** Temperature T. **b** Gradient of temperature $T_{,y}$

6 Conclusions

In this work, we propose the SFEM based on the framework of finite element method but incorporating a strain-smoothing technique used in Galerkin mesh-free method. The strain field is projected onto a constant field or set of constant fields based on smoothing cells within the element. Compared with the conventional FEM using four-node isoparametric elements, SFEM shows the following features.

(1) Field gradients are computed directly only using shape functions itself and no derivative of shape function is needed, which accordingly reduce the requirement on the smoothness of shape functions. The shape functions are created in a trivial, simple and explicit manner. High-order field gradients can be evaluated accurately by recursive application of the non-local gradient operation.
(2) Depending on the requirement on the accuracy and stability, an element may be further subdivided into finite number of smoothing cells. In particular, a quadrilateral element divided into four smoothing cells can avoid the spurious zero-energy mode. A smoothing operation is conducted over each cell. If a constant smoothing function is used, area integration over a cell can be recast into line integration along its edges.
(3) Unlike the conventional FEM using isoparametric elements, as no coordinate transformation or mapping is performed in SFEM, no limitation is imposed on the shape of elements used herein. Even severely distorted elements are allowed. Domain discretization is more flexible than FEM.
(4) The convergence rate in displacement of SFEM is comparable with that of FEM while its energy generally converges faster than that of four-node bilinear finite elements. The numerical results of SFEM are generally more accurate than FEM, though the same post-processing technique is used to smooth the strains and stresses. The computational cost of the SFEM is roughly less expensive than the FEM especially for domain divided by a very large number of elements.

(5) SFEM has been implemented using tile elements and polygonal elements, where the standard FEM is not applicable.

Several numerical examples are studied and their results are in good agreement with analytical solutions. The accuracy and convergence are demonstrated through numerical results. The method is easy to implement. As no coordinate transformation is involved, the procedure of SFEM is more straightforward than the isoparametric FEM. The method is very robust and versatile. So far we did not encounter any restrictions on this method other than material incompressibility.

Though only 2D elastic problems are considered in this work, there is no difficulty to extend the application of SFEM to other relatively complicated problems, such as 3D problems, geometric and elasto-plastic nonlinear problems, etc. Necessary theoretical foundations need to be laid in future work including its relationship with FEM mixed formulations. Error analysis and convergence study in theory will also be conducted and compared with existing numerical methods.

References

1. Bathe KJ (1996) Finite element procedures. Prentice Hall, New Jersey
2. Beissel S, Belytschko T (1996) Nodal integration of the element - free Galerkin method. Comput Meth Appl Mech Eng 139:49–74
3. Belytschko T, Lu YY, Gu L (1994) Element-free Galerkin methods. Int J Numer Method Eng 37:229–256
4. Belytschko T, Krongauz Y, Organ D, Fleming M, Krysl P (1996) Meshless Method: An Overview and Recent Developments. Comput Meth Appl Mech Eng 139:3–47
5. Bonet J, Kulasegaram S (1999) Correction and stabilization of smooth particle hydrodynamics methods with applications in metal forming simulation. Int J Numer Method Eng 47:1189–1214
6. Chen JS, Wu CT, Belytschko T (2000) Regularization of material instabilities by meshfree approximations with intrinsic length scales. Int J Numer Method Eng 47:1303–1322
7. Chen JS, Wu CT, Yoon S, You Y (2001) A stabilized conforming nodal integration for Galerkin meshfree method. Int J Numer Method Eng 50:435–466
8. Dai KY, Liu GR, Lim KM, Gu YT (2003) Comparison between the radial point interpolation and the Kriging based interpolation used in mesh-free methods. Comput Mech 32:60–70
9. Krongauz Y, Belytschko T (1997) Consistent pseudo-derivatives in meshless method. Int J Numer Method Eng 146:371–386
10. Li Y, Liu GR, Luan MT, Dai KY, Zhong ZH, Li GY, Han X (2006) Contact analysis for solids based on linearly conforming RPIM. Comput Mech (in press)
11. Liu GR (2002) Mesh-free methods: moving beyond the finite element method. CRC Press, Boca Raton
12. Liu GR, Li Y, Dai KY, Luan MT, Xue W (2006a) A linearly conforming RPIM for 2D solid mechanics. Int J Comput Methods (in press)
13. Liu GR, Quek SS (2003) The finite element method: a practical course. Butterworth Heinemann, Oxford
14. Liu GR, Zhang GY, Dai KY, Wang YY, Zhong ZH, Li G, Han X (2006b) A linearly conforming point interpolation method (LC-PIM) for 2D solid mechanics problems. Int J Comput Methods (in press)
15. Liu WK, Jun S, Zhang YF (1995) Reproducing kernel particle methods. Int J Numer Method Eng 20:1081–1106
16. Monaghan JJ (1982) Why particle methods work. Siam J Sci Sat Comput 3(4):423–433
17. Sukumar N (2004) Construction of polygonal interpolants: a maximum entropy approach. Int J Numer Method Eng 61:2159–2181
18. Sukumar N, Moran B (1999) C^1 natural neighbor interpolation for partial differential equations. Numer Methods Partial Differential Equations 15:417
19. Sukumar N, Moran B, Belytschko T (1998) The natural element method in solid mechanics. Int J Numer Method Eng 43:839–887
20. Sukumar N, Tabarraei (2004) Conforming polygonal finite elements. Int J Numer Method Eng 61:2045–2066
21. Timoshenko SP, Goodier JN (1970) Theory of elasticity, 3rd edn. McGraw-Hill, New York
22. Wang JG, Liu GR (2002) A point interpolation meshless method based on radial basis functions. Int J Numer Method Eng 54:1623–1648
23. Yoo JW, Moran B, Chen JS (2004) Stabilized conforming nodal integration in the natural-element method. Int J Numer Method Eng 60:861–890
24. Zienkiewicz OC, Taylor RL (2000) The finite element method, 5th edn. Butterworth Heinemann, Oxford